JGR Space Physics

Two Techniques for Determining F-Region Ion Velocities at Meso-Scales: Differences and Impacts on Joule Heating

Andrew J. Kavanagh[1,2] , Yasunobu Ogawa[3] , and Emma E. Woodfield[1]

[1]British Antarctic Survey, Cambridge, UK, [2]Visiting Scientist at RAL Space, Rutherford Appleton Laboratory, Oxford, UK, [3]National Institute for Polar Research, Tokyo, Japan

Abstract We have investigated the difference between two standard techniques for deriving the ionospheric ion velocity using data taken with the EISCAT incoherent scatter radar between 1987 and 2007. For large-scale convection flows, there is little difference between the tristatic and monostatic techniques, though the biggest relative difference occurs during periods when the interplanetary magnetic field (IMF) is strongly northward. At small scales the difference between the two techniques is correlated with a measure of the variability of the tristatic measurement. This suggests that small-scale flow bursts, such as those associated with enhanced auroral arcs, could explain the local time variation in the velocity difference distributions. The difference in velocities obtained from the monostatic and tristatic techniques can make a significant difference in the estimate of the magnitude of Joule heating in the thermosphere. Considering only the electric field dominated component of Joule heating, Q, the difference in the two techniques can be as much as 52% of the tristatic measurement ($Q_m = 0.48Q_t$) in the morning sector (0–6 MLT), during a moderate to large geomagnetic storm. This reduces to a difference of 36% at non-storm times in the same MLT period. Careful averaging of the velocity field with the future EISCAT_3D radar system will allow us to establish the impact of both spatial and temporal scales on the magnitude of the observations.

Plain Language Summary We compare two different methods of using an ionospheric radar to measure the speed of ions moving through the high-altitude ionosphere. One method measures over a shorter time and smaller space than the other. We find that although both methods show similar large-scale patterns (100–1,000s of km) in the velocity at different times of day and for different levels of space weather driving, there can be large differences at small scales (10–100s of km). This can affect estimates of the heating of the atmosphere that are important for understanding satellite drag, for example. The difference in heating can be very large at certain times of day (nearly double).

1. Introduction

To understand the electrodynamics of the ionosphere, it is essential to know the behavior of the ionospheric electric field. This determines the drift of particles in the geomagnetic field, it is a key component in driving ionospheric currents and it strongly affects the levels of ionospheric heating. Consequently, it is an important factor in assessing the pathways by which space weather impacts technology and society.

The electric field can be measured by satellites (e.g., Gustafsson et al., 1997; Rich & Hairston, 1994) and can also be estimated indirectly from the ground using radars (e.g., Chisham et al., 2007; Rishbeth & Williams, 1985). Since the electric field is related to the plasma velocity in the ionosphere and the local magnetic field, a measurement of the plasma motion will yield an estimate of the electric field by assuming that the ion-neutral collisions are negligible, which is reasonable at a sufficiently high altitude (Brekke et al., 1994), in the F region of the ionosphere.

There are several types of ionospheric radar but in their simplest form they all work in essentially the same manner: the radar transmits a signal that is scatted by some structure in the ionosphere and the received signal is doppler shifted due to the motion of the structure, which is assumed to move with the bulk plasma motion. For coherent scatter radars these targets are field-aligned irregularities that are convected via the ExB drift motion (Tsunoda, 1988), combining measurements from multiple radars can provide 2-D horizontal vectors (e.g., Hanuise et al., 1993; Ruohoniemi & Baker, 1998). Incoherent Scatter Radar (ISR) signals reflect from ion-acoustic waves, giving a small-scale measurement of the ion velocity in the direction of the radar beam. ISR with at least three

spaced receivers can provide 3-D vectors and the European Incoherent Scatter Radar (EISCAT) is unique in having such a tristatic capability (Rishbeth & Williams, 1985).

A second method for retrieving vectors is to use a single radar and look in multiple directions (the monostatic technique), combining the resultant line of sight velocities into a vector (e.g., Foster, 1983; Hagfors & Behnke, 1974; Zhang et al., 2007). Phased array radars such as the AMISR (Heinselman & Nicolls, 2008) can do this relatively quickly, as they are capable of digitally generating multiple beams. This monostatic measurement is also possible using a single dish antenna that can be steered to different pointing directions; this method has also been employed to derive altitude profiles of the ion velocity, something that is not easily done with a traditional tristatic approach (Williams et al., 1984).

These techniques have different strengths and weaknesses, and the velocity estimates that are produced depend strongly on the assumptions that are made. The scanning monostatic technique depends on assuming stationarity in the ionospheric plasma for the duration of a scan. The tristatic method relies on retrieving a weaker signal at remote receiver sites (weaker due to the distance from the scattering target).

The technique used for determining the velocity has implications for the potential applications. For example, using the monostatic technique to estimate the electric field during a period of dynamic, changing auroral structure could result in an underestimate as the relatively slow scan and large spatial area will act to filter out rapid flow bursts or strongly localized flows (e.g., Williams et al., 1989). Similarly, estimates of the electric field that rely on averaging over time and space will also lead to lower values, whichever the measurement technique. This can have a significant impact on estimates of electrodynamic properties, such as the current density or the level of Joule heating across the ionosphere (e.g., Rodger et al., 2001). Thus, it is important to ascertain the reliability of the underlying velocity estimate and determine whether any subsequent analysis might require a "correction" factor to improve their ability to capture the global picture (e.g., global scale models of electric field).

In this paper we use data from three decades of operations of the EISCAT tristatic radar to study the difference between the tristatic method and the scanning monostatic method. The tristatic measures at a scale of ∼10 km in the F region, whilst the monostatic measures across ∼100 km, due to the scanning motion. We show that at times the two methods show good overall agreement in their trends, but that large variability exists both in the tristatic method and in the relationship between the two techniques. This variability is partially controlled by geomagnetic activity levels. We consider a particular case period and examine the effect of the two techniques on the ionospheric component of Joule Heating. The monostatic method underestimates the tristatic by as much as 20%–40%.

2. Instrumentation

The EISCAT Association operates several ionospheric radars and support instruments in the European arctic. This study uses data provided by the UHF (ultra-high frequency) radar situated in Ramfjordmoen, near Tromsø, in northern Norway (69.58°, 19.23°, geographic coordinates). The EISCAT UHF operates on frequencies around 930 MHz using a 32 m, mechanically steerable, parabolic dish. It primarily measures ionospheric parameters above ∼70 km altitude, with basic range and temporal resolution dictated by the chosen pulse length (1 μs–10 ms). The UHF transmits and receives on the same antenna providing profiles of ionospheric parameters. Until 2012 it could also operate in tristatic mode, where the back scattered signal was detected by two remote receiver stations at Sodankylä, Finland (67.37°, 26.63°) and Kiruna, Sweden (67.87°, 20.43°). Combining the data from the receivers allowed vector measurements to be resolved, along with the standard profiles of electron density, electron temperature, ion temperature and the line-of-sight ion velocity (Williams et al., 1984). Post 2012 the tristatic capability was switched to the co-located VHF radar, due to increased interference from commercial use in the UHF radio band. Unfortunately, the VHF radar cannot be scanned in azimuth and has highly limited elevation control. In the future EISCAT_3D will incorporate multiple tristatic measurements.

An alternative method for extracting velocity vectors is through scanning the radar dish through several dwell positions and then calculating the velocity vector based upon the line-of-sight velocities recorded at each dwell position. Compared to the tristatic method this has the drawback of requiring a longer measurement period to compile a single velocity estimate; however, it does allow a profile of velocity vectors to be resolved giving a
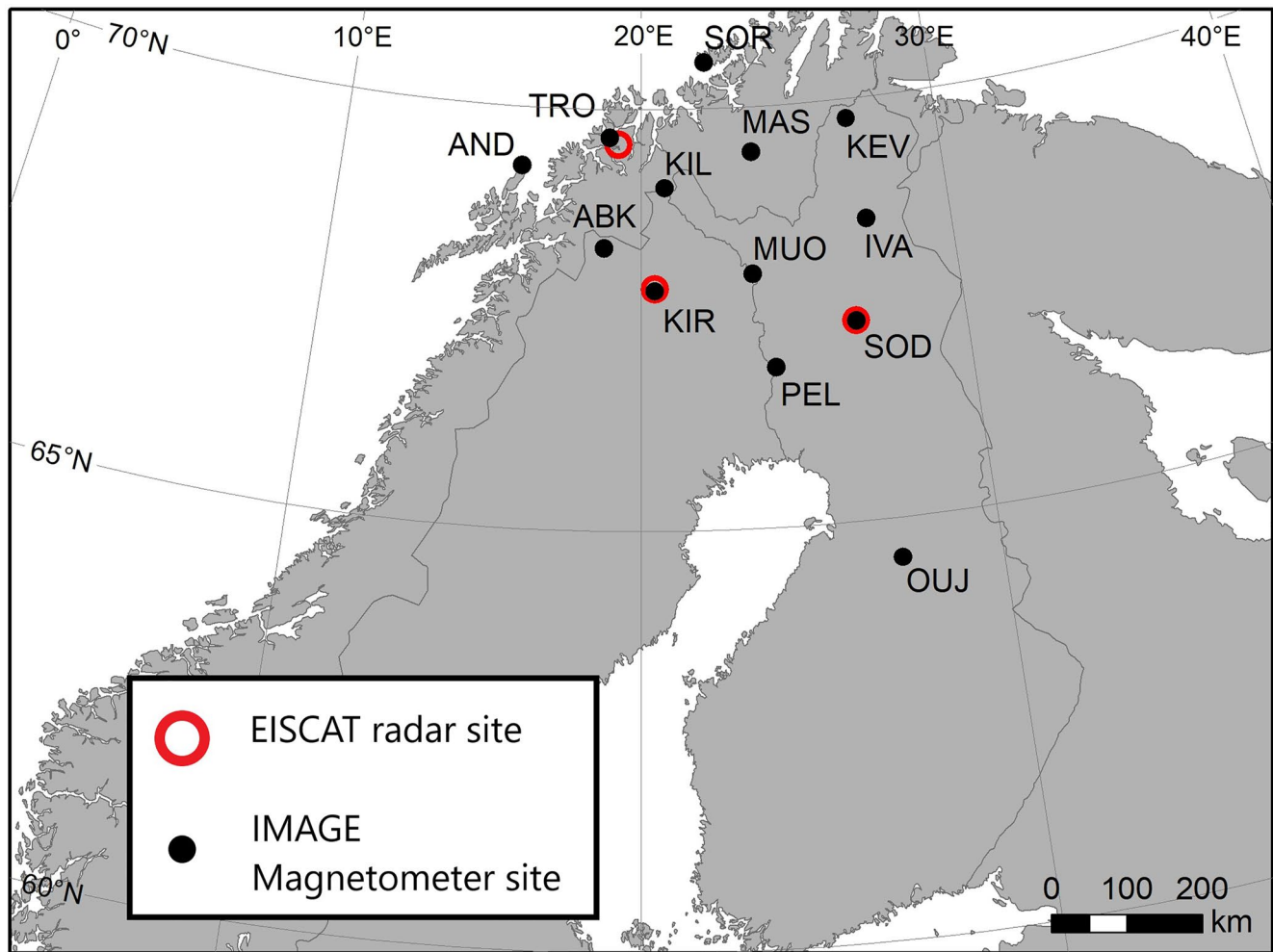
Figure 1. Locations of the European Incoherent Scatter (EISCAT) radar sites (red circles) at Tromsø, Kiruna and Sodankylä. Locations of International Monitor for Auroral Geomagnetic Effects (IMAGE) magnetometer stations (black dots) that have contributed to the calculation of the IE index used in this study.

means of probing the change with altitude and for estimating the neutral wind velocity (Nozawa & Brekke, 2000; Nygrén et al., 2011)

EISCAT radar measurements are converted into ionospheric parameters, including velocity estimates, using the Grand Unified Incoherent Scatter Design and Analysis Package (GUISDAP), maintained by EISCAT (Lehtinen & Huuskonen, 1996). This software package is available for anyone to download from the EISCAT website. Essentially theoretical spectra derived from model estimates of the ionospheric parameters are fitted to the autocorrelation function (ACF) of the received signal. From this process estimates of the ionospheric plasma density, electron and ion temperatures and the line-of-sight ion velocity are obtained. The results are usually calibrated against a local measurement of the plasma frequency from EISCAT's own Dynsasonde (Wright & Pitteway, 1979a, 1979b). A detailed description of EISCAT and its capabilities is available in Rishbeth and Williams (1985) and Rishbeth and van Eyken, (1993).

Figure 1 shows the locations of the EISCAT UHF radar sites at Tromsø (TRO), Sodankyla (SOD) and Kiruna (KIR) as red circles. It is worth noting that since 2012 the remote receiver sites have been re-tasked to operate with the VHF radar that operates from Tromsø, maintaining EISCAT's tristatic capability. The black circles in Figure 1 indicate the locations of some of the International Monitor for Auroral Geomagnetic Effects (IMAGE) network of magnetometers. These magnetometers measure the magnetic field at ground level and are sensitive to changes in the ionospheric current sheet (Lühr et al., 1998); they enable us to place EISCAT observations in the context of varying geomagnetic activity. In this study, we use the IE indicator; this is a local version of the

Auroral Electrojet (AE) index. The AE index is derived from 12 observatories distributed longitudinally to give a global-scale measure of substorm-driven activity (Davis & Sugiura, 1966); in this study the IE indicator is determined from these IMAGE magnetometers to provide a more local scale measure.

Alongside IE we also consider the response of the EISCAT measurements to the driving solar wind conditions, particularly the interplanetary magnetic field (IMF). IMF data have been taken from the OMNI database (King & Papitashvili, 2005; Papitashvili & King, 2020); these data are collated from several spacecraft upstream of Earth the solar wind and propagated to the nose of the bow shock. To allow for comparison with the measurement in the ionosphere we have adjusted the timing of the IMF data by an average 13 min to account for the delay across the magnetosheath and to the ionosphere (Khan & Cowley, 1999).

3. Data Description

The EISCAT radars do not take data continuously, but instead operate in campaign mode; half of the time they perform bespoke, user defined experiments known as Special Programmes (SP) and for the other half they run a series of standard experiments known as Common Programmes (CP). The latter cover a range of different pointing directions and scans to investigate different processes, but with the aim of building a synoptic data set. In this study we have used data from the Common Programme 2 (CP2) experiment from between 1987 and 2005 (inclusive); this is a scanning experiment where the radar dwells in four directions defined by azimuth and elevation pairs: (180°, 90°), (183°, 77°), (167°, 64°), and (133°, 61°). The total scan takes 360 s with an average dwell time of 60 s. The pointing values are representative since the exact directions have changed by small amounts over the years to maintain a magnetic field-aligned position (the second direction in the set above).

For this work, all the monostatic measurements are taken from range gates centered between 240 and 255.5 km altitude, where the height of the gates is 20–30 km. This is in the F-layer, far removed from the collision dominant E-region, thus the electric field will tend to be the dominant driver of the measured velocity rather than the neutral wind. The neutral wind does still contribute to the ion velocity, particularly over longer times and larger spatial scales, but abrupt temporal and spatial changes in the velocity are reasonably attributed to changes in the electric field. Occasionally the interaction height of the tristatic measurement is changed, usually due to the magnitude of the electron density in the F layer; if it is too weak then the returned radar signal would be insufficient to analyze on a reasonable time scale. This is particularly important for the remote sites, which are a significant horizontal distance away and as such are attempting to receive a weaker scattered signal. Given the density drops away above the F-layer peak, it is advisable to set the interaction height close to where the density maximizes (depending of course on the aims of the experiment). At all times, the tristatic interaction height lay within the width of the altitude gate range of the monostatic measurement and given the scale height of the F-region the difference can in general be ignored. The horizontal scale of the tristatic measurement is defined by the beam width of the radar and the interaction region with the remote beams, giving ∼10 km. The positions of the dwell points in the radar scan pattern defines the horizontal scale of the monostatic method and the largest distance is ∼135 km. Thus, the two techniques are measuring the ion velocity across at least an order of magnitude difference.

Figure 2 shows (a) the extent of the data in time and how it is distributed as a function of (b) month and (c) magnetic local time (MLT). Panel (a) shows the number of data points in each calendar month for the period from 1987 to 2005 (inclusive), represented by black bars. Overlaid is a 30-day running median of the daily sunspot number (dashed blue line) showing when the data were taken with respect to the solar cycle. A significant fraction of the CP2 experiments occurred across solar cycle 22 (1986–1996) with fewer observations in solar cycle 23 (1996–2008). The EISCAT mainland radars underwent a refurbishment in 2000–2001 limiting their operation, also the CP2 runs form only one of several common programmes, and at times, other experiments take precedence. The large spike in 2005 was due to a dedicated month-long CP2 run in September and was during the declining phase of the solar cycle, which tend to be geomagnetically active (e.g., Tsurutani et al., 2006).

Panel (b) breaks the observations down by time of year showing that the coverage by season was not uniform, with much fewer CP2 observations in the winter months than the Summer and particularly Autumn. CP2 is only one of a suite of common programmes operated by EISCAT, which include fixed field-aligned positions, low altitude D-region, low elevation monitoring of the polar region and large-scale scans to sample more of the ionosphere. The common time is often balanced between these experiments and so there are further limits to the amount of time operated by the radar in CP2 mode. The numbers here refer to the tristatic measurements and in
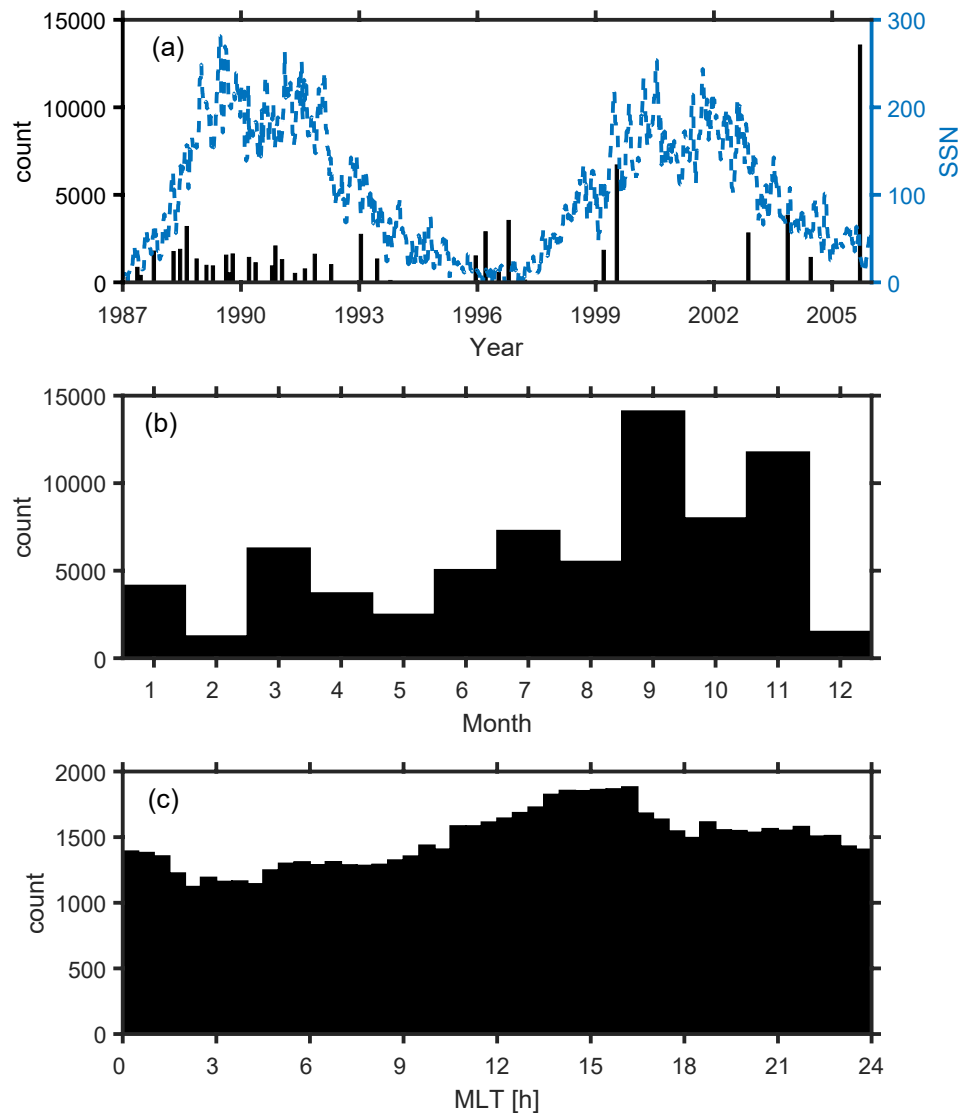
Figure 2. European Incoherent Scatter Radar (EISCAT) tristatic velocity data occurrence as a function of (a) year, (b) month and (c) Magnetic Local Time. Panel (a) shows the counts per calendar month as black bars; overlaid is the averaged sunspot number (dashed blue line–right Y axis), to show how the data distribution relates to the solar cycle. In (b) the columns represent the amount of data per month (aggregated across all years). Common Programme 2 (CP2) observation in any given year depend on the special time experiments run and which common programmes are used. Panel (c) shows the amount of data in each 30-min bin of magnetic local time (MLT). There is a tendency to peak in the post-noon sector.

general there are four of these for every monostatic measurement. Panel (c) gives the occurrence as a function of magnetic local time (MLT). The data are sorted into 30-min bins. There is good local time coverage with a peak in the afternoon sector and a minimum pre-dawn. There are times when one or both techniques will fail and produce a bad data point, for example, if the signal-to-noise ratio is too low. If GUISDAP indicates a poor fit in the analysis, those data have been discarded along with the corresponding data from the other technique (Lehtinen & Huuskonen, 1996). Only data where a full vector has been resolved (north, east, and upward components) have been retained. No attempt has been made to remove data above a threshold value unless there was an obvious problem (such as a step-change in the time series due to unflagged analysis errors). This could lead to unfeasibly large velocity vectors that might be described as "unphysical." However, given the maximum velocity possible in the ionosphere is an unknown quantity we have not created a potentially artificial limit. Aikio et al. (2018) reported flow channels with velocities of 3,300 ms^{-1}, measured by EISCAT and the SWARM satellites, which was above previous expectations of a peak velocity. The frequency width of the radar receiver is wide enough that
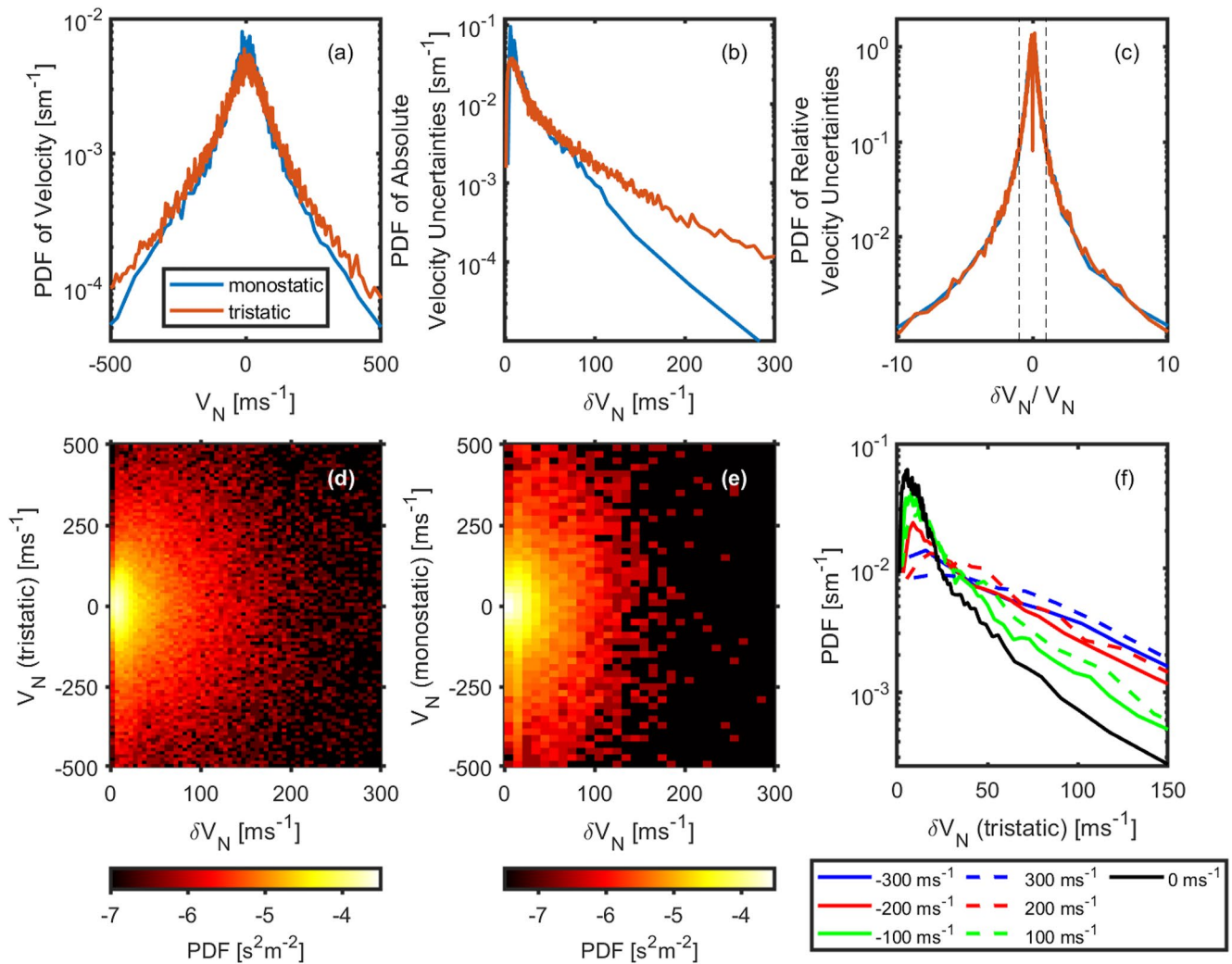
Figure 3. Probability Distribution Functions (PDFs) of the northward velocity (a), the associated uncertainties (b), and the relative uncertainties (c). In each case the blue (orange) line shows the data from the monostatic (tristatic) technique. The second row shows the distribution of velocity as a function of the uncertainty for the tristatic (d) and monostatic (e) techniques. The last panel (f) provides a comparison of the PDF of the tristatic uncertainty sampled across a range of velocities centered on the values indicated in the legend. Each PDF includes data from $V_N \pm 20 \text{ ms}^{-1}$.

it is highly unlikely that any high velocities are the result of aliasing. Overall, this leaves 71,098 useable tristatic data points and 19,308 monostatic data points (at a given altitude) between 1987 and 2005 (inclusive).

In Figure 3 we look more closely at the uncertainties associated with the data using the northward component (V_N) as an example (the other components behave similarly). Uncertainties (or errors) on the velocity measurements are calculated during the analysis of the incoherent scatter spectrum where the GUISDAP software uses the variance of the deviation of the observed and predicted lags of the ACF to derive an estimate of the random error (e.g., Williams et al., 1996). Errors are propagated and combined via the analysis package when vector velocities are derived. Panel (a) shows the probability distribution function (PDF) of the ion velocity for the monostatic (blue) and tristatic (orange) techniques. The latter has a broader distribution indicating that it responds to higher velocities. In panel (b) we show the PDF of the associated uncertainties which illustrate that the tristatic method has a higher probability of a higher uncertainty.

For the tristatic measurements the uncertainties are a combination of the errors associated with the velocities measured by the UHF (as described above) and the two remote sites. For the line-of sight velocity the biggest factor is the signal-to-noise ratio, which is dependent on the plasma density and the distance along the radar beam. The distance to the remote receivers is large (see Figure 1) and this will naturally lead to larger uncertainties. In

panel (c) we show the relative errors; these are broadly symmetrical around zero and the two dashed lines indicate where $\delta V_N = V_N$. 90% of the data (both techniques) have $V_N > \delta V_N$ (and 82% have $V_N > 0.5 \times \delta V_N$, 56% have $V_N > 0.1 \times \delta V_N$). The relationship between the velocity value and associated error is explored in panels (d–f). The 2-D PDF of the velocity as a function of the uncertainty for the tristatic and monostatic techniques are shown in panels (d and f) respectively. Both show very similar responses such that there is no simple linear relationship between the two; high velocity is not always associated with high uncertainty, though the paucity of data at high values may mask the effect. The peak close to $\delta V_N = 0$ that is pronounced below ± 200 ms^{-1}, smooths out at higher speeds. In panel (f) we have plotted the 1-D PDF for selected velocities (each value in the legend is the center value with ± 20 ms^{-1}). The black line is for $V_N = 0$ ms^{-1} and as we move to higher speeds (both northward and southward), the tails of the distribution do increase, such that there is an increased likelihood of larger uncertainty at higher velocities. For example, at 200 ms^{-1} there is an approximate order of magnitude difference between an uncertainty close to zero and a value close to 150 ms^{-1}, this difference decreases slowly as we move to larger velocities.

In the following analysis we will compare averages of the ion velocity data both on small and large temporal scales. Data with large uncertainties can skew averages, especially when looking at the impact of small-scale high velocities. Given the weak relationship between δV and V illustrated in panel (f) of Figure 3, using a median value rather than a simple mean will partially offset any impact of the high velocity values, but will also tend to undermine the contribution of high velocity data with low uncertainty. Therefore, to account for the uncertainty we haves used the weighted means both for analysis of the bulk flow and for directly comparing the monostatic and tristatic measurements.

In 2007 a new CP2 scan pattern was implemented with shorter scan and dwell times, and different pointing directions, in effect creating a different experiment. We decided to focus on the older configuration since it had significantly more data. A preliminary analysis of the second scan suggested it yielded similar results to those presented here.

4. Analysis

In this section we consider how the estimates of ion velocity vary in magnetic local time and in response to solar wind driving. Although it is possible to look at the statistical differences between the two data sets direct comparison of the two techniques is made difficult due to the inherent temporal resolution differences between them. To overcome this, we use two approaches: we compare the probability distribution function of the ion velocity; and we use a value of the tristatic measurements averaged to the same resolution as the monostatic estimate (i.e., the weighted mean of the tristatic velocity in each monostatic scan). The latter technique leads to some smoothing of the variability of the tristatic estimate and so we also look at an additional parameter as a measure of that variability: the difference between the highest and lowest tristatic values in each scan (ΔV_t).

4.1. Bulk Motion

Figure 4 presents the probability distribution functions (PDFs) of the ion velocity data. Each column represents a different velocity component: V_E, eastward (left), V_N, northward (middle) and V_U, upward (right). In panels (a–c) the blue (orange) line is the monostatic (tristatic) ion velocity distribution. The bin sizes are fixed and indicated on the plots. Although curtailed at the edges, each plot contains more than 94% (84%) of the monostatic (tristatic) data.

The distributions are similar but with differences in each component. Both techniques result in wide distributions, but the tristatic is most likely to measure higher velocities, especially noticeable in V_N and V_U. Both the tristatic and monostatic measurements in panel (a) show an asymmetry, with a large bump on the westward (negative) tail. The color panels (d–i) show the 2-dimensional PDFs, splitting the velocity data into hourly bins of MLT; the same color scales are used for both monostatic and tristatic in each column. Panels (d–f) show the tristatic distributions, with panels (g–i) showing the monostatic; the yellow, white and blue lines show the median, mean and weighted mean respectively, whilst the dashed line gives the 0 ms^{-1} position for reference. There is a well-defined local time dependence, with strong changes in the shape of the distribution between dayside and nightside for all components, for both techniques. There is a large broadening in V_E with greater skew to negative values starting in the afternoon sector before switching positive across midnight.
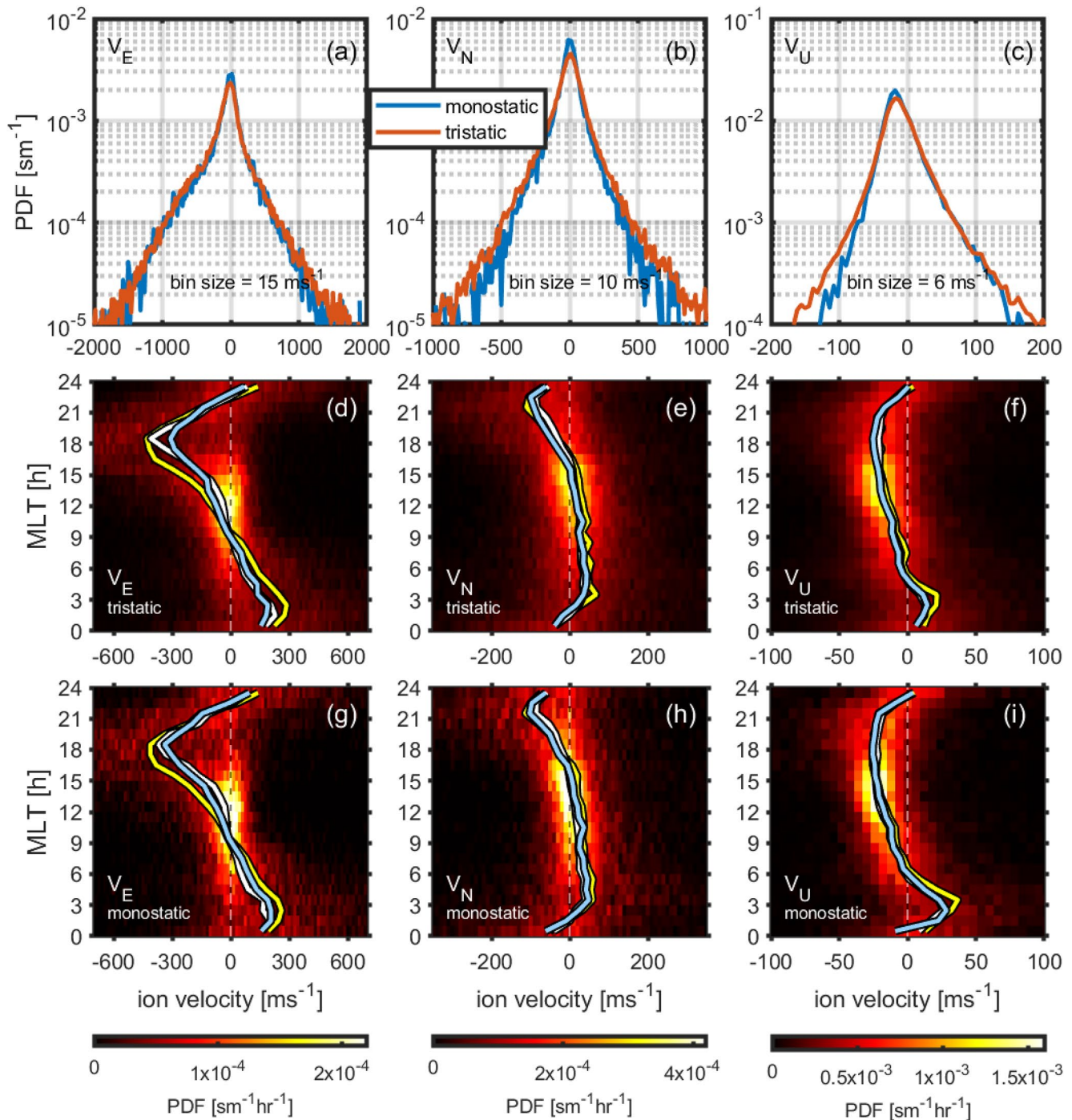
Figure 4. Probability Distribution Functions (PDFs) of the ion velocity. The top three panels show the PDFs for the eastward (a), northward (b) and upward (c) components for the monostatic (blue) and tristatic (orange) velocities. Bin sizes are indicated in each plot. The tristatic has a broader distribution with longer tails indicating a tendency for high velocities. Panels (d–i) show the PDFs as a function of magnetic local time, high-lighting that both tristatic and monostatic are strongly dominated by the large-scale ionospheric velocity pattern. The yellow, white, and light blue lines in each plot shows the median, mean and the weighted mean velocity for each hour of local time.

The similar bulk pattern for each technique reflects the overall large-scale velocity structure of the ionosphere, dominated by convection. However, the monostatic measurements have narrower distributions with sharper peaks across a larger range of MLT. That the two techniques produce broadly similar results is reassuring that they are capturing the overall velocity structure well. Given the range of possible values in each MLT, it is natural to

wonder how the level of geomagnetic activity affects the two techniques, and by how much the two methods vary relative to each other at a given time. The large-scale convection pattern is driven by the solar wind and interplanetary magnetic field (IMF) via reconnection (Dungey, 1961). The changes in driving will be responsible for some of the spread in the distributions since variations in the IMF will alter the location and rate of reconnection (e.g., Trattner et al., 2005), which in turn alters the overall convection pattern (e.g., Ruohoniemi & Greenwald, 2005).

Figure 5 presents weighted mean values of the horizontal ion velocity sorted by MLT and the clock angle of the IMF, θ_{IMF}, which is defined as the angle of the field from north, in the north-east plane (Y-Z in GSM coordinates). It is positive clockwise, negative in the anti-clockwise sense. Vectors have been calculated from the weighted means of V_E and V_N in each 1-hr bin of MLT for four different IMF conditions: (a) $|\theta_{IMF}| < 45°$, or northward; (b) $135° < |\theta_{IMF}|$, or southward; (c) $135° > \theta_{IMF} > 45°$, or eastward; and (d) $-135° < \theta_{IMF} < -45°$, or westward.

The arrows give the magnitude and direction for the tristatic, V_t, (orange) and monostatic, V_m, (blue), where northward is to the top of the plot and eastward is to the right of the plot. The black arrow in the bottom right corner of each panel gives the scale of the vectors; it should be noted that these vary with northward (Figure 5a) being the smallest (50 ms^{-1}) and southward (Figure 5b) being the largest (200 ms^{-1}) The small dial-plot in the bottom left-hand corner of each panel shows the number of monostatic data points behind each vector in the larger plot (multiply by 3.7 to get the approximate tristatic data numbers). The data have been split by IMF direction to separate the dominant drivers of reconnection. Under northward IMF, lobe reconnection can occur, but the strength of driving of the flow is generally reduced. For southward IMF convection is strongly enhanced and larger flows will cover a greater region. The B_Y component can modify the convection pattern, skewing the size and locations of the cells. Freeman et al. (1993) showed that lobe reconnection can begin at $\theta_{IMF} \sim \pm 45°$, hence the chosen boundaries of our bins.

Average ion velocities under northward IMF (a) are much lower than for southward conditions (b); however, the relative differences in direction and magnitude are larger for northward than for southward though the absolute velocity differences are similar between the two IMF directions (<25 ms^{-1}). Exceptions occur for northward IMF at 1–2 MLT (>65 ms^{-1}), 16–18 MLT (>34 ms^{-1}) and 22 MLT (34 ms^{-1}); and for southward IMF at 2 MLT (88 ms^{-1}), 10 MLT (86 ms^{-1}) and 14–15 MLT (>43 ms^{-1}). Northward IMF conditions (a) led to much larger and variable differences in direction through MLT with small periods of consistent direction change. For southward IMF (b) the difference in direction are much smaller (averaging ~6° compared to 20° for northward IMF). This is consistent with strong driving from steady reconnection; though these are snap-shot values, and no attempt has been made to select based on persistence of IMF direction. The patterns of flow direction for the eastward (c) and westward (d) IMF are similar, though the magnitudes vary. There are moderate magnitude differences between the two techniques either side of midnight for both IMF directions. The angular differences are relatively small at all MLT, the highest being close to noon and pre-midnight in both cases.

4.2. Small Scales

Both techniques capture the overall bulk motion of the ionosphere when considering large-scale averages (in space and time), though the biggest difference occur under northward IMF. Moving beyond the bulk motion, we consider the relationship between V_m and V_t at the small-scale.

Figure 6 shows the ion velocities from the 13 September 2005. This day was part of a quasi-continuous 20 days run of the EISCAT UHF. These data have also been analyzed in other work (e.g., Aikio et al., 2012; Cai et al., 2014). The top two panels present the solar wind and geomagnetic activity for the interval. Panel (a) shows the IMF B_Y (black) and B_Z (red) components. Through the interval the IMF rotated from predominantly eastward to westward, with a varying southward component prior to 14 UT. After this the IMF had a mostly northward component, but with southward excursions at ~18:30 UT and 22:30 UT. In Panel (b) the local electrojet indicator, IE, shows several peaks corresponding to the changes in the IMF, including a particularly broad peak between 9 and 14 UT, which is linked to a period of strongly southward IMF. The magnetic local time at EISCAT leads UT by approximately 2 hr, such that activity at 12 UT is close to 14 MLT.

Panels (c–e) show the ion velocity components for the tristatic (orange) and monostatic (blue) methods. Here we have included an averaged tristatic value (green); this is the arithmetic weighted mean of the tristatic values across each scan, such that one averaged tristatic value corresponds to a single monostatic value. This allows a one-to-one comparison of the two methods. For each estimate of the velocity the overall structure
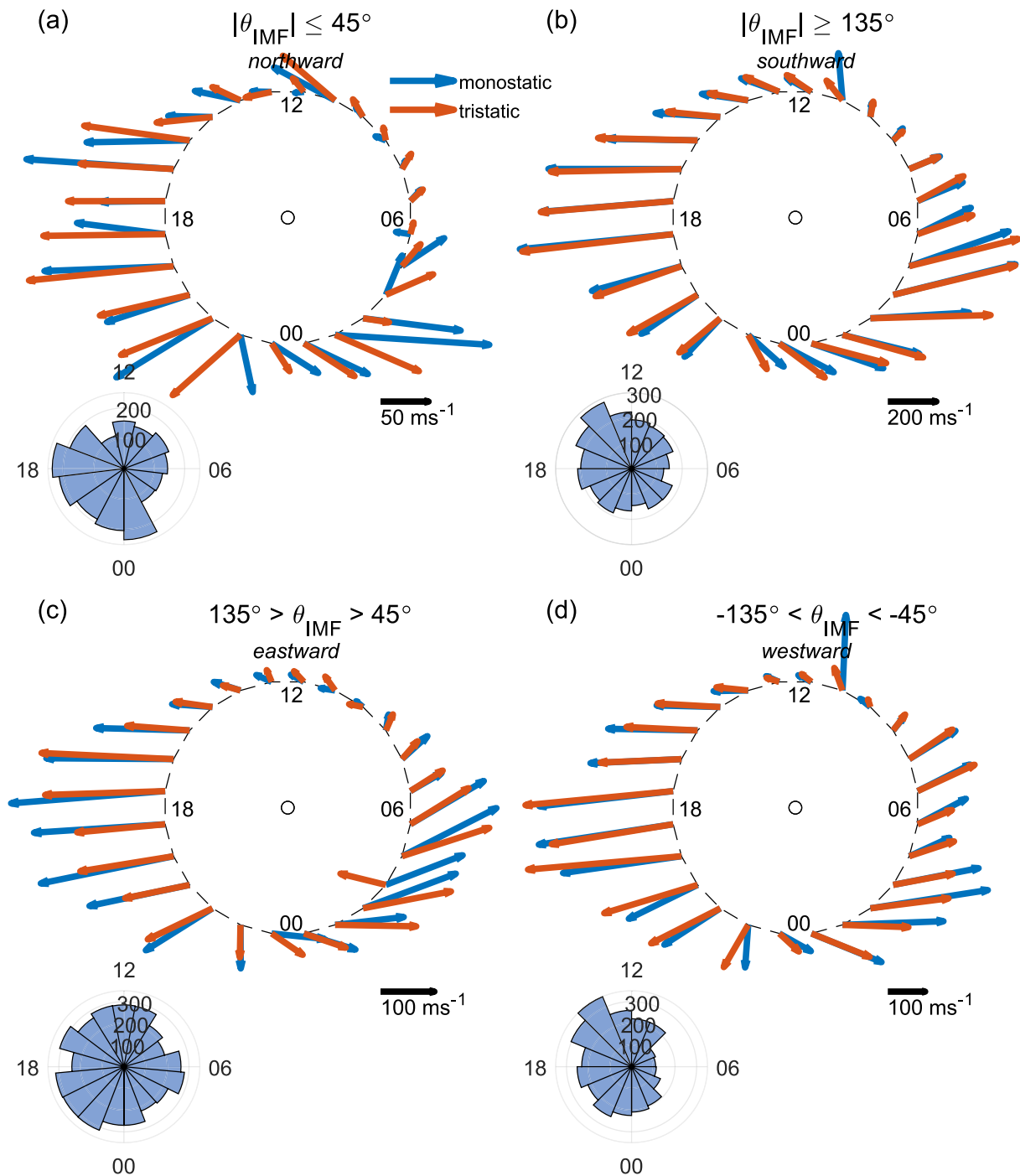
Figure 5. Clock plots showing the vectors of the weighted mean horizontal velocity in each 1-hr bin of magnetic local time (MLT) for the monostatic (blue) and tristatic (orange) measurements for different interplanetary magnetic field (IMF) conditions. The blue bar plots show the amount of data behind the averages in each bin. The single black vectors indicate the scale size for each plot. (a) northward IMF where the absolute clock angle is less than 45°; (b) southward IMF where the absolute clock angle is greater than 135°; (c) eastward IMF, with clock angle between 45° and 135°; (d) westward IMF, with clock angle between −45° and −135°. The positive (negative) clock angle is measured (anti)clockwise from north GSM. The northward IMF shows a lot of difference between the techniques, notably in angle as well as magnitude. Note that the absolute magnitude differences are similar in each plot.

throughout the day is broadly similar. All three values show large westward flows across noon in response to the peak in the broad IE and the southward IMF. There is large variability in each component, standing out in V_N (d), V_U (e) and in V_E (c) though the scale masks this (due to the large change in the bulk motion). There are periods of large variability including large differences between the different methods. The largest
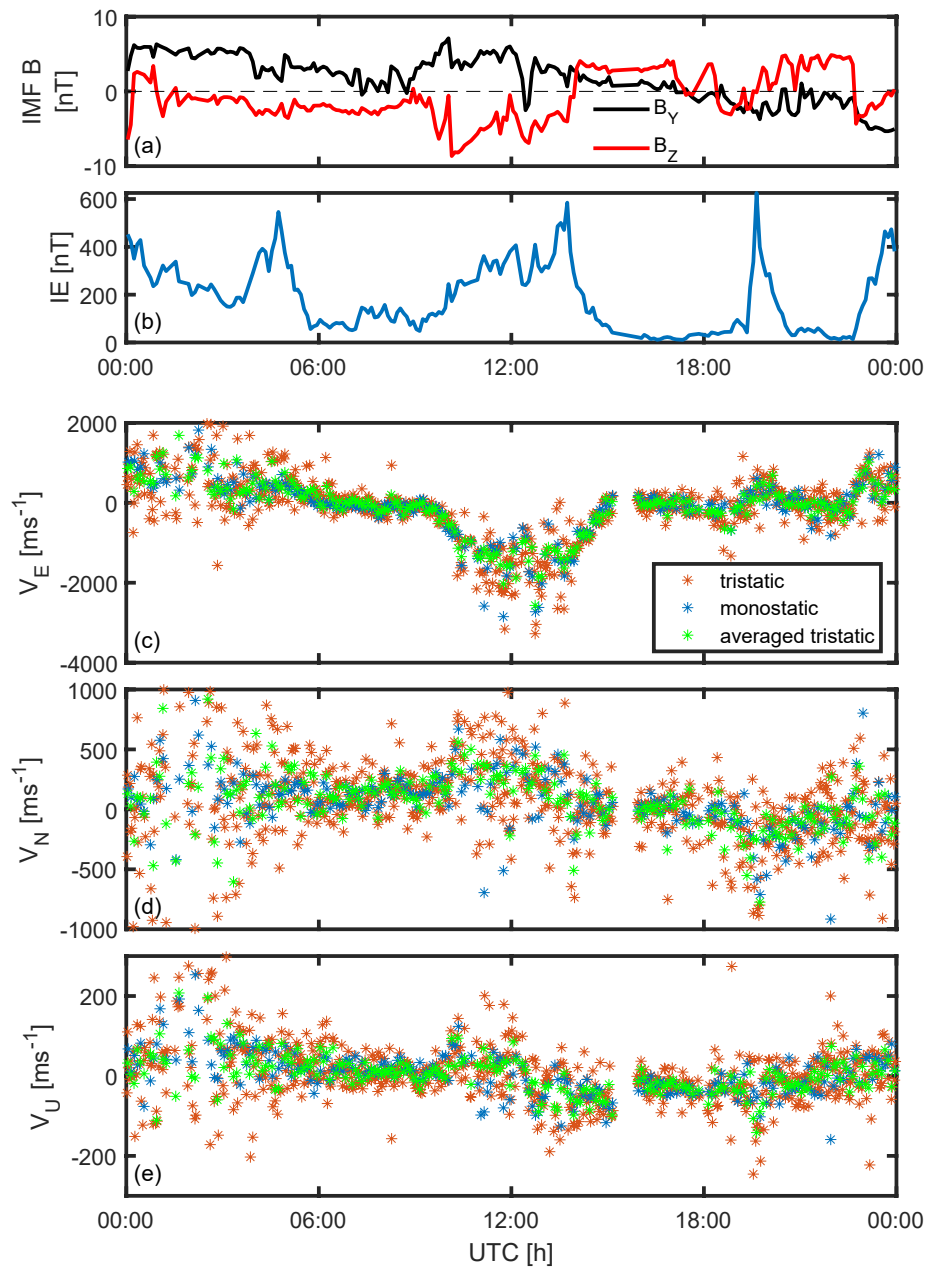
Figure 6. Observations on the 13 September 2005, the radar was running the CP2 scan pattern. (a) the interplanetary magnetic field (IMF) B_y (black) and B_z (red) from the OMNI database. (b) the IE indicator (a local measure of AE) derived from the magnetometer stations shown in Figure 1. (c) the eastward component of the ion velocity for the tristatic (orange), monostatic (blue) and averaged tristatic (green) measurements. (d) as for (c) but for the northward component. (e) as for (c) but for the upward component. Each component shows more variability during active periods, with the tristatic showing the most. Overall variability increases during geomagnetically active periods.

coincides with the enhanced IE values, both on the night-side and to a lesser degree on the dayside. This is reflected in all components. It is not clear from these data whether there is any systemic difference or variability.

In Figure 7 we explore the inherent variability in the tristatic measurement. The top panel (a) once again shows the corresponding IE index. The lower three panels show the eastward (b), northward (c) and upward (d) components for two parameters derived from the ion velocities: black dots represent the difference between the monostatic and average tristatic measurements, $V_m - V_{tav,}$ (left hand axis); the filled line is the difference between the

maximum and minimum values of the tristatic velocity, ΔV_t, within a single scan (right-hand axis). The tristatic values are from different points within the monostatic scan and as such the variability, ΔV_t, represents a mixture of spatial and temporal effects. The difference between the monostatic and tristatic measurements show larger variability with increases in magnitude during periods of enhanced geomagnetic activity for all components.

The distribution of $V_m - V_{tav}$ is close to symmetric about zero with a mean of 0.31 ms^{-1} for V_E, 0.53 ms^{-1} for V_N and -0.03 ms^{-1} for V_U (the medians are approximately an order of magnitude higher). However, the distribution has heavy tails and so the standard deviation is very large (448 ms^{-1} for V_E). If we consider the absolute value of the difference, $|V_m - V_{tav}|$, the mean is 179 ms^{-1} for V_E, and the difference in probability density is within an order of magnitude of the 0 ms^{-1} difference. Comparing the monostatic and tristatic velocity values in this way illustrates that there are significant differences at the small scales, even when the larger trends are similar. For example, 12% of the data points show opposite directions in the V_E component, 17% in the V_N component and 12% in the V_U component across the entire data set.

The variability of the underlying tristatic measurement is represented by the ΔV_t parameter. Figure 7 indicates that this value also increases (for each component) as geomagnetic activity is enhanced; like $V_m - V_{tav}$ the relationship is not linear, since similar levels of IE can produce a weaker or stronger response in ΔV_t. This suggests a complex relationship that may involve an effect due to the different response of the ionosphere at different MLT, and of course may reflect the shift in location relative to the convection pattern. That said the two parameters, $|V_m - V_{tav}|$ and ΔV_t, are weakly correlated (for V_E) in the interval shown with $R = 0.33$ (upper and lower bounds of 0.44 and 0.20 for the 95% confidence interval). However, when the entire dataset is considered, this correlation increases such that $R = 0.59$ (upper and lower bounds of 0.60 and 0.58 for the 95% confidence interval). Thus, larger differences in the two techniques are linked to periods when the tristatic measurement experiences large variability on short time scales.

Figure 8 shows the distributions of $V_m - V_{tav}$ (a, b) and ΔV_t (c, d) as a function of MLT for the V_N component; the white lines represent the median values in each MLT bin. The data have been separated by the orientation of the IMF clock angle, for the northward (a, c, e) and southward (b, d, f) directions. The bottom two panels show the underlying counts in each MLT bin.

For $V_m - V_{tav}$ the distributions narrow close to noon and widen on the nightside and the median values would suggest a small difference between northward and southward IMF conditions (>50 ms^{-1} at all MLT). However, the distributions in all MLT are wider for southward IMF, which suggests that not only are bigger differences more likely on the nightside, but the differences increase under stronger driving and/or active conditions. Similar results occur for ΔV_t, though this time the difference is clearer in the median values. The distributions suggest higher probability of increased variability in the short-term tristatic measurement on the nightside, and this probability increases with southward IMF. Very similar distributions for both parameters can be achieved by sorting the data by the IE index.

Given the strong dependence on MLT, particularly the variability on the nightside it is worth considering whether solar illumination may play a role. This was ruled out as a strong effect by comparing the distribution of ion velocity as a function of solar elevation angle and splitting the data into dayside and nightside MLT regions to show the resultant distributions are different (Figure S1 in Supporting Information S1).

5. Discussion

The EISCAT radars provide a unique method for comparing two techniques for determining the ion velocity in the ionosphere. The two techniques, although often considered interchangeable, are measuring across different spatial and temporal scales. The tristatic measurement has a horizontal scale of ~10 km, whereas the monostatic measures across ~100 km. The tristatic method gives a rapid measurement, limited only by the integration time required to achieve sufficient signal (from seconds to minutes); the monostatic method provides a slower measurement (few to 10s of minutes) that by its nature smooths across a larger portion of the sky and relies on the local conditions not changing over the time span of the measurement. In this sense the monostatic technique acts as a natural filter for small scale (spatial and/or temporal) phenomena (Williams et al., 1990). To date EISCAT has been the only radar with tristatic capability so that other incoherent scatter radars have had to rely on some version of the monostatic technique or beam swinging to derive an ion velocity vector, and an estimate of the
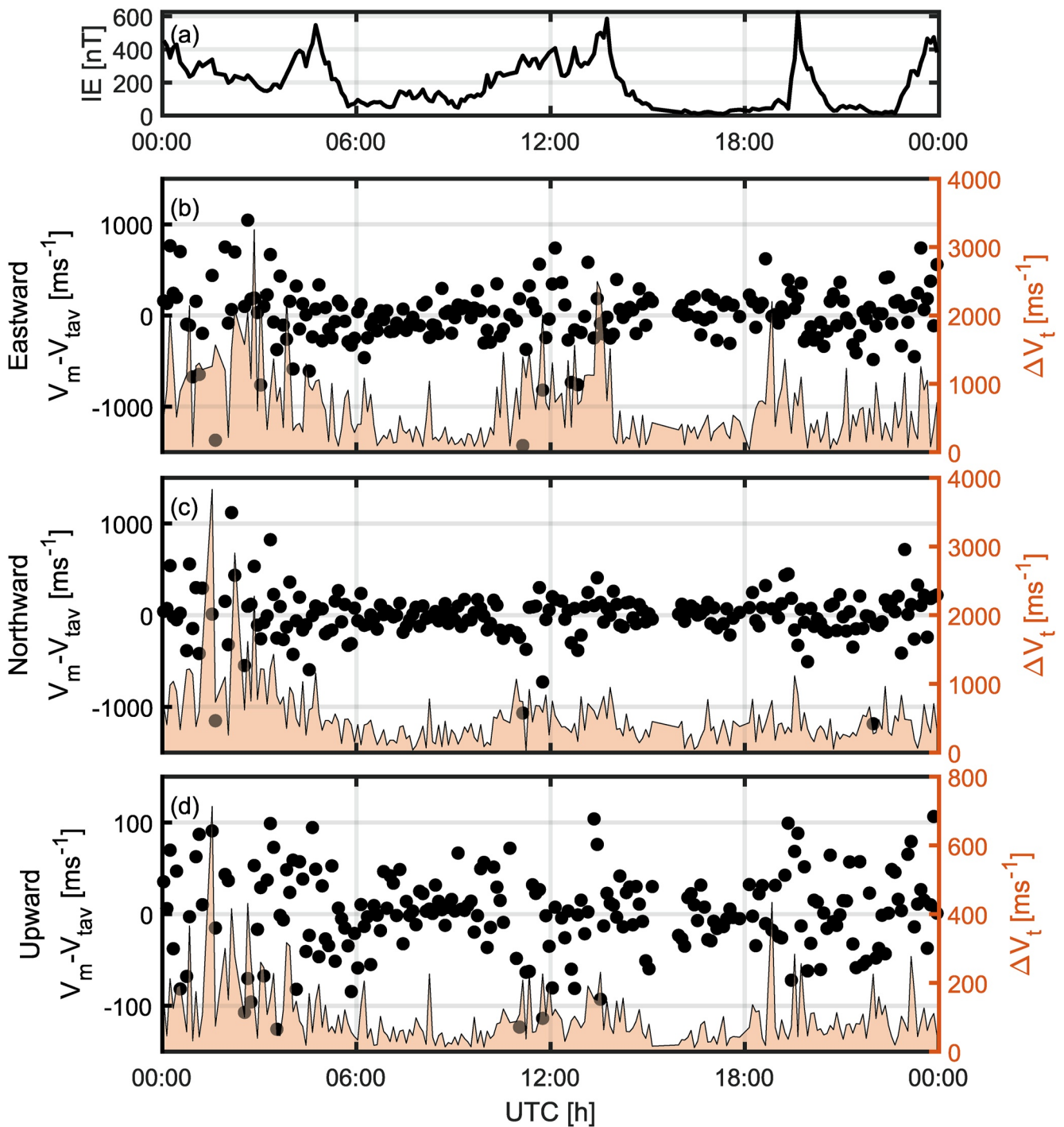
Figure 7. (a) the IE indicator as in Figure 4. Panels (c–d) show the difference between the monostatic and averaged tristatic velocity (black circles) for the eastward (b), northward (c) and upward (d) components. The shaded regions show the difference between the maximum and minimum values of V_t that underlie each value of V_{tav} (right y-axis). This gives a measure of the variability of the data. Both the difference and the variability go up during active periods. The averaged tristatic velocity retains significant differences with the monostatic.

ionospheric electric field (e.g., Behnke & Hagfors, 1974). Therefore, it is important to understand how the two techniques relate to each other and whether the monostatic method is adequately capturing important detail of flows in the ionosphere (if it is assumed that the tristatic measurement more accurately reflects the true conditions at small scales). Given that other techniques may also rely on averaging over longer timescales and/or larger
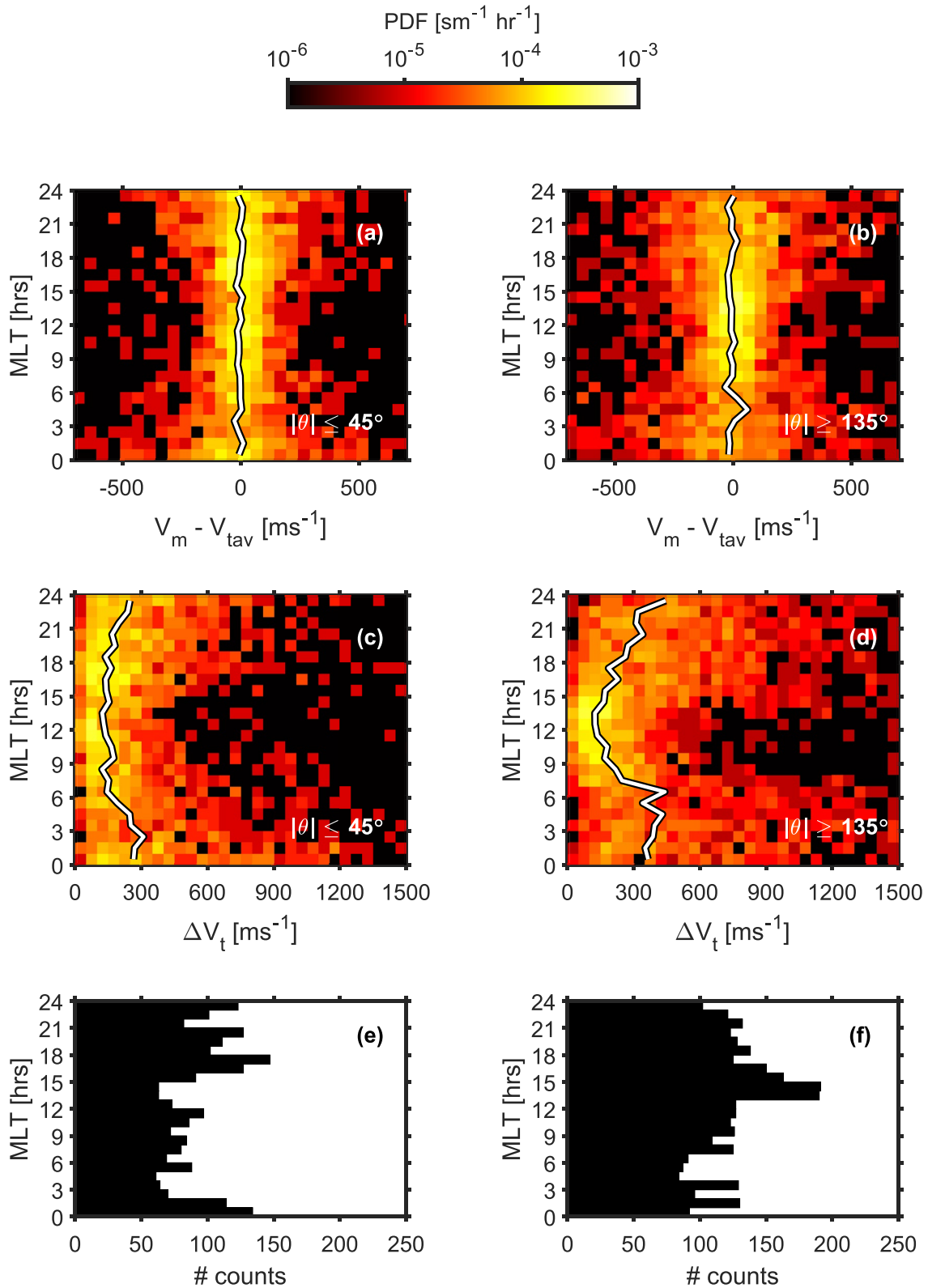
Figure 8.

areas/volumes this provides an insight into how important it may be to determine a correction factor to capture small scale variation.

Williams et al. (1984) were the first to examine the two techniques, using data from 18 May 1982. They found generally good agreement in the overall structure, though there were clear differences in the velocity, both in magnitude and direction. For parts of the day the difference in the northward component was as much as 200 ms^{-1}. In this current study we found similar results to Williams et al. (1984), but with considerably more data we were able to consider how the two velocity estimates responded to different levels of solar wind driving/geomagnetic activity and to examine the variation in local time.

EISCAT velocity data has been compared with other techniques for measuring ionospheric flow velocities, most notably observations from the high frequency (HF) Hankasalmi, Finland, radar of the Super Dual Auroral radar Network (SuperDARN) (e.g., Davies et al., 1999; Gillies et al., 2010). These studies used the UHF tristatic velocity to calculate the component velocity along the SuperDARN beam. Davies et al. (1999) found a reasonable correspondence and explained the observed differences in terms of contamination of the SuperDARN data with scatter from the E-region and some issues with the spatial and temporal sampling. Gillies et al. (2010) found a good correlation but found the SuperDARN velocities to be lower than those measured by EISCAT. This was attributed to an overestimate of the refractive index in the HF coherent scattering region.

The advent of phased array ISR has allowed quicker monostatic measurements, partially removing the problem of rapidly changing conditions (Heinselman & Nicolls, 2008), though retaining the spatial averaging. The arrival of EISCAT_3D, a tristatic phased array capable of multiple beam intersections (McCrea et al., 2015) at high power, will improve our ability to examine both the spatial and temporal response of the velocity field to changing conditions.

The data presented in Figure 6 illustrates a large variability in the velocity measurements as well as big differences between V_m and V_t for all components of the ion velocity. These data are like those presented by Williams et al. (1984) in their Figure 5. In both cases there is a broad agreement in the overall trends for each component, but there are substantial differences in velocity at a given time from the two techniques. Figure 3 showed the distribution of the associated errors, that are derived in the analysis of the incoherent scatter spectrum. To determine if there is a substantial difference between the two techniques, we compare the velocities and associated uncertainties for the monostatic and the averaged tristatic values to calculate the percentage of data points where the two values overlap. that is,

$$(V_{tav} - n\delta V_{tav}) \leq V_m \pm n\delta V_m \leq (V_{tav} + n\delta V_{tav}) \tag{1}$$

$$(V_m - n\delta V_m) \leq V_{tav} \pm n\delta V_{tav} \leq (V_m + n\delta V_m) \tag{2}$$

where δV is the associated uncertainty (or error) and n is an integer value allowing us to scale the breadth of the uncertainty window to determine the overlap. For the entire data set the percentage of data where the uncertainties overlap ($n = 1$) are 36% of V_E and 42% of V_N. If we accept that the distribution of errors is such that wider bounds are more reasonable (e.g., $n = 2$) then the amount of overlap increases to 61% for V_E, and 69% for V_N. Therefore, we conclude that the difference in the two techniques is important and worth considering in more detail.

5.1. Bulk Motion

The tristatic and monostatic techniques result in very similar distributions in MLT (Figure 4) showing that both techniques capture the same overall motion. The velocity distributions are wide, non-gaussian, not centered around zero, and have large skew, particularly on the nightside. Although not shown, the shape of the distributions in MLT do change with the prevailing IMF conditions, consistent with studies of the convection pattern (Ruohoniemi & Greenwald, 2005). Sorting the data by IMF B_Z has the biggest effect, with negative values leading

Figure 8. Distribution of $V_m - V_{tav}$ and ΔV_t (northward component) as a function of magnetic local time (MLT) for northward (left panels) and southward interplanetary magnetic field (IMF) (right panels). Panels (a and b) show the Probability Distribution Functions (PDFs) for the difference in velocity between the monostatic and averaged tristatic values. Panels (c and d) show the PDFs for the difference in velocity within each scan, again as a function of MLT. The white lines indicate the median values. The direction of the IMF makes very little difference to $V_m - V_{tav}$ in MLT, though the distribution is broader for southward IMF (b). The same is true for ΔV_t, with a much larger difference on the night-side. The bottom two panels (e, f) show the number of data points behind each MLT bin. MLT bins are 1 hr wide, velocity bin widths are 50 ms^{-1}.

to wider, more skewed distributions and positive B_Z reducing them slightly. Either way, neither the mean nor median values are necessarily good representations of the flow at a given time. This emphasizes the danger of relying on simple empirical models to provide ionospheric flows and related parameters (e.g., the electric field).

There are differences: the tristatic distribution is heavier tailed perhaps suggesting that it is more responsive to faster streams in the ionosphere than the monostatic. These would be either smaller spatial and/or temporal scales. In Figure 5 we explicitly looked at the effect of the IMF direction by binning the data both by the clock angle and MLT and calculating weighted means for both V_m and V_t. The resultant average velocities are in good agreement with those presented by Cai et al. (2014), who used a sub-set of EISCAT data to examine ion velocities at two latitudes for different clock angles, though using different boundary values for the bins.

Although there are clearly differences in the overall velocity patterns between IMF orientations, it is when we compare the velocity estimates under a given orientation that we find an interesting feature. There are small to moderate differences between V_t and V_m for southward (b), eastward (c) and westward (d) IMF, but there are large differences in both the magnitude and angle of V_t and V_m at virtually all MLT under northward IMF (a). This result is similar to the findings of Abel et al. (2009) who used SuperDARN data to assess the effect of IMF clock angle (θ_{IMF}) on ionospheric velocity across different scales (between ~45 and ~1,200 km). Abel et al. (2009) found that when the IMF was nearly purely northward the velocity fluctuations were different to all other orientations. They attributed this to the influence of solar wind driving in all cases except for northward IMF where the ionosphere is "decoupled from the solar wind." Some caution should be employed when attributing our results to the same cause as those suggested by Abel et al. (2009) since their observations were limited to open field lines in the polar cap, whereas the EISCAT observations are likely to be nearly always on closed field lines. Abel et al. (2006) reported observing different behavior either side of the open-closed boundary (OCB), though they only considered the effect of the IMF on data poleward of the OCB. However, that strong coupling tends to lead to similar values for V_t and V_m whilst weaker driving results in differences in variability at different scales is a reasonable conclusion.

It is worth noting a further limitation in this analysis. We have used instantaneous measurements of the IMF (as propagated from the solar wind to the bow shock and with a fixed 13-min traversal time to the ionosphere), consequently there is no consideration of how variable the IMF was at a given time and the impact on the ionospheric velocity. Ideally periods of quasi stable IMF would have been identified and the corresponding velocity data binned appropriately, but the sporadic, non-continuous, synoptic nature of the EISCAT measurements makes this analysis extremely difficult on the scales we are looking at. This does mean that there is a large uncertainty surrounding the measurements that we have presented but we have constrained this by using somewhat large IMF bins, such that the consequences of the intermittency of the IMF is mostly contained within the bins.

We have established that the direction of the IMF not only impacts the overall bulk motion (as we would expect) for the velocity derived from both techniques, but that it also effects the relationship between the velocity estimates. Although the biggest relative effect was when the IMF was northward, all other directions still have periods when the difference between V_t and V_m is appreciable. For the eastward and westward IMF cases, the difference between V_m and V_t tends to be more variable between ~21 and 05 MLT, and particularly stable in the dusk sector.

5.2. Small Scale Motion

In Figure 6, we used data from the 13 September 2005 to provide a snapshot example of how the V_t and V_m related to each other and also introduced V_{tav} to allow direct numerical comparison. Both V_m and V_t showed considerable variation with geomagnetic activity linked to changes in the IMF, as did V_{tav}, which did partially bridge the gap between the two techniques, but still retained considerable difference with V_m. This was highlighted in Figure 7 where the difference between V_m and V_{tav} were presented for the same period along with a measure of the variability of V_t within a given value of V_{tav}, ΔV_t. There was considerable spread in the velocity difference, which tended to increase during periods of high geomagnetic activity; ΔV_t was also more variable during the same active periods. This would seem to be the opposite result to the conclusion of the bulk motion analysis, which suggested that quieter times (i.e., northward IMF) led to bigger differences.

In Figure 8 the analysis was expanded to the larger dataset, which confirmed the variability as a function of IMF direction but also indicated an MLT effect. The distributions of $V_m - V_{tav}$ were wider on the nightside though

more so for southward IMF (b) than for northward (a). The same is true for ΔV_t, which shows a much narrower distribution around noon. We were able to rule out solar illumination as a significant contribution to this MLT effect (see Supporting Information S1), such that the tristatic velocity tends to be more variable on the nightside, especially for southward IMF and this accompanies bigger differences in V_m–V_{tav} (a weak correlation between the two parameters does exist, $R = 0.59$). A possible explanation is that the tristatic measurement is responding to short duration/spatially confined flows missed by the slower, larger scale monostatic measurement.

The nightside of the ionosphere is linked to the tail of the magnetosphere and consequently it is home to the footprints of variable geomagnetic processes and dynamic current systems. The most notable manifestation of these processes is the aurora and auroral arcs have strong electric fields associated with them which in turn will lead to variable ion flows. Short duration flow bursts have been observed associated with auroral intensifications (e.g., Zou et al., 2009) as well as longer duration bursty bulk flows (e.g., Grocott et al., 2004). Phenomenon such as these certainly lead to variability in the nightside ionospheric flow on different scales. Williams et al. (1989) described short bursts of plasma velocity during substorms from EISCAT observations. Williams et al. (1990) used a combination of scanning tristatic and monostatic measurements to investigate bursts on the nightside and found that they were short-lived (3–7 min) and not always well detected by the monostatic mode. They did find examples where the velocity was well correlated over 1° of latitude such that the main limitation was the temporal rather than spatial extent of the measurement. These bursts were observed across the nightside of the ionosphere (Williams reported mostly in the evening and midnight sectors, but inspection of their data show a significant amount post-midnight). This is a plausible candidate for driving the difference between V_m and V_{tav}.

5.3. Electrodynamic Consequences

It is worth considering the impact that the differences between the two velocity estimates will have on our assessment of electrodynamic processes in the ionosphere. Joule heating is a significant effect of energy exchange between the magnetosphere, ionosphere and thermosphere. Authors have provided varying descriptions of how the process works (e.g., Strangeway, 2012; Vasyliunas & Song, 2005) but fundamentally it is caused by the dissipation of energy in ionospheric currents, associated with the electric field. The resistivity that leads to current dissipation is due to the collisions between the ions and neutrals, such that the overall temperature of both species is increased. Accurate estimates of Joule heating are important both for understanding the energy budget of the magnetosphere-ionosphere system and for the dynamics of the thermosphere. For example, large scale heating of the high latitude atmosphere will result in increased density at higher altitudes, which in turn will increase the atmospheric drag that is imparted to satellites and space debris that pass through, and hence change their orbital characteristics. To predict satellite orbit perturbations, we need good estimates of the neutral density, which rely on good estimates of the heating.

Rodger et al. (2001) found a median 20% (upper limit of 40%) underestimate of Joule heating when comparing hourly averaged electric field with 6-min averages. It is worth determining how much further that underestimation may go when looking at even smaller scales, especially when many estimates of Joule heating will necessarily rely on large scale observations. Deng and Ridley (2007) showed that model resolution made a big difference to estimates of the heating; changing the resolution from 5° to 1.25° latitude led to a 20% increase in heating. They suggested that this in-turn was an underestimate since it relied on averaged and smoothed empirical models of the electric field. Deng et al. (2009) used an empirical model with an electric field variability component to investigate the influence of this variability on Joule heating. They found that the variability increased the heating by more than 100%.

Aikio et al. (2012) provide a good summary of the electromagnetic energy exchange rates that result in Joule heating (Q_J) and show that it can be calculated for a height interval between altitudes z_1 and z_2 by the integral:

$$Q_J = \int_{z_1}^{z_s} \sigma_p \left(\boldsymbol{E} + (\boldsymbol{U} \times \boldsymbol{B}) \right)^2 \mathrm{d}z \qquad \left(\text{Watts m}^{-2} \right) \tag{3}$$

where $\boldsymbol{B}$ is the magnetic field, $\boldsymbol{U}$ is the height dependent (z) neutral wind field and σ_p is the height dependent Pedersen conductivity. E is the ionospheric electric field in the Earth-fixed frame of reference, and is given by:

$$\boldsymbol{E} = -\boldsymbol{V} \times \boldsymbol{B} \qquad \left(\text{Vm}^{-1} \right) \tag{4}$$

where V is the ion velocity.

If the neutral wind is neglected, then we can simplify Equation 3 and express the "ionospheric" Joule heating as

$$Q = \Sigma_P E^2 \qquad \left(\text{Watts m}^{-2} \right) \tag{5}$$

where Σ_P is the height integrated Pedersen conductivity, or conductance. Σ_P can be determined from the EISCAT electron density and temperature values (e.g., Senior et al., 2007); in this instance we have used values in the NIPR EISCAT database (http://pc115.seg20.nipr.ac.jp/www/eiscatdata/), following the method outlined in Hosokawa and Ogawa (2010). Σ_P is obtained for each dwell position in each scan, which will introduce some error due to the radar positioning being non-field aligned. For our purposes this should be sufficiently small that it can be ignored. For the monostatic data time series, Σ_P has been interpolated to give one value per scan. The magnetic field, B, is obtained from the International Geomagnetic Reference Field (IGRF) (Thébault et al., 2015).

Q is not the absolute value of Joule heating, rather it is an estimate of the "ionospheric" component and ignores the neutral component. Although including the effect of the neutral motion of the atmosphere is important for determining the absolute heating values (Billett et al., 2019; Thayer, 1998) in this case we are comparing two different methods over the same time interval. The neutral motion can be estimated from optical instruments (Aruliah et al., 2010) or by a combination of the EISCAT tristatic and lower altitude monostatic measurement (Nozawa & Brekke, 2000). In this instance the same correction would be applied to both the monostatic and tristatic techniques. Thus, the heating values that we discuss are not absolute and the most important consideration is the difference between the two outputs.

We can apply Equations 4 and 5 to derive estimates of the Joule heating rate from both the monostatic and tristatic velocities and compare the two results. Figure 5 indicated both a local time and geomagnetic activity effect on the differences between V_t and V_m, reinforced in Figure 8. Therefore, we would expect that the link between Q from tristatic and monostatic would show both an MLT and geomagnetic effect. During the long CP2 run that EISCAT operated in September 2005, there was a large geomagnetic storm, which peaked on the 11 September 2005 (maximum IE = 1500 nT) followed by a quiet period from the 18 September 2005.

In Figure 9 we present a comparison of the storm with the non-storm period by considering the average of Q as a function of MLT. Panel (a) shows the median IE for the storm (black circles) and non-storm (red crosses) periods. Panel (b) shows the corresponding averaged hourly values of Joule heating for the tristatic, Q_t (orange), and monostatic, Q_m, (blue), techniques, with dashed lines representing the "non-storm" periods. These are weighted means, using the associated errors from the velocity estimates; this reduces the impact of data with large uncertainties, but retains the inherent variability of the data that would be lost when considering median values. Panel (c) gives the relative difference of Q from the two methods, normalized to the tristatic value and panel (d) shows that the number of data points in each bin are broadly similar for each technique.

Both monostatic and tristatic techniques follow the same diurnal pattern, very similar to that shown by Cai et al. (2014), including the suppression of the afternoon peak for geomagnetically quieter periods. Overall, Q_t is greater than Q_m, particularly in the morning sector and more so for the storm-time conditions. There are two points where $Q_m > Q_t$, at 3 MLT and 18 MLT, both during the non-storm time with the latter when Q was very low. In general, the non-storm Q track each other quite closely. Overall, the median relative difference between the two techniques is 45% (48%) of Q_t during storm-time (non-storm time), this rises to 52% for the peak period (0–6 MLT) during the storm but drops to 36% in the non-storm period. Differences are very similar across noon, but during the secondary peak after 14 MLT the difference is only 26% of Q_t, though the daytime values for Q during the non-storm period are exceptionally low. Plots of the median of Q as a function of MLT are provided for comparison in the supporting material (Figures S2 and S3 in Supporting Information S1). These show that the interquartile range strongly overlap in the afternoon sector, suggesting these values are broadly similar, but in the morning sector the tristatic range is much larger.

As stated above, these values of Joule heating (Q) are only the ionospheric component (that part dominated by the electric field) and ignore the effect of the neutral winds (Equation 3). The contribution of the neutral wind to Joule heating as has been studied by previous authors (e.g., Aikio et al., 2012; Fujii et al., 1999) and shown to have an MLT and geomagnetic activity dependence. During medium to high geomagnetic activity winds tend to increase heating rates in the mornings sector (by 20%–30%) but decrease them in the evening. Assuming a 30% increase
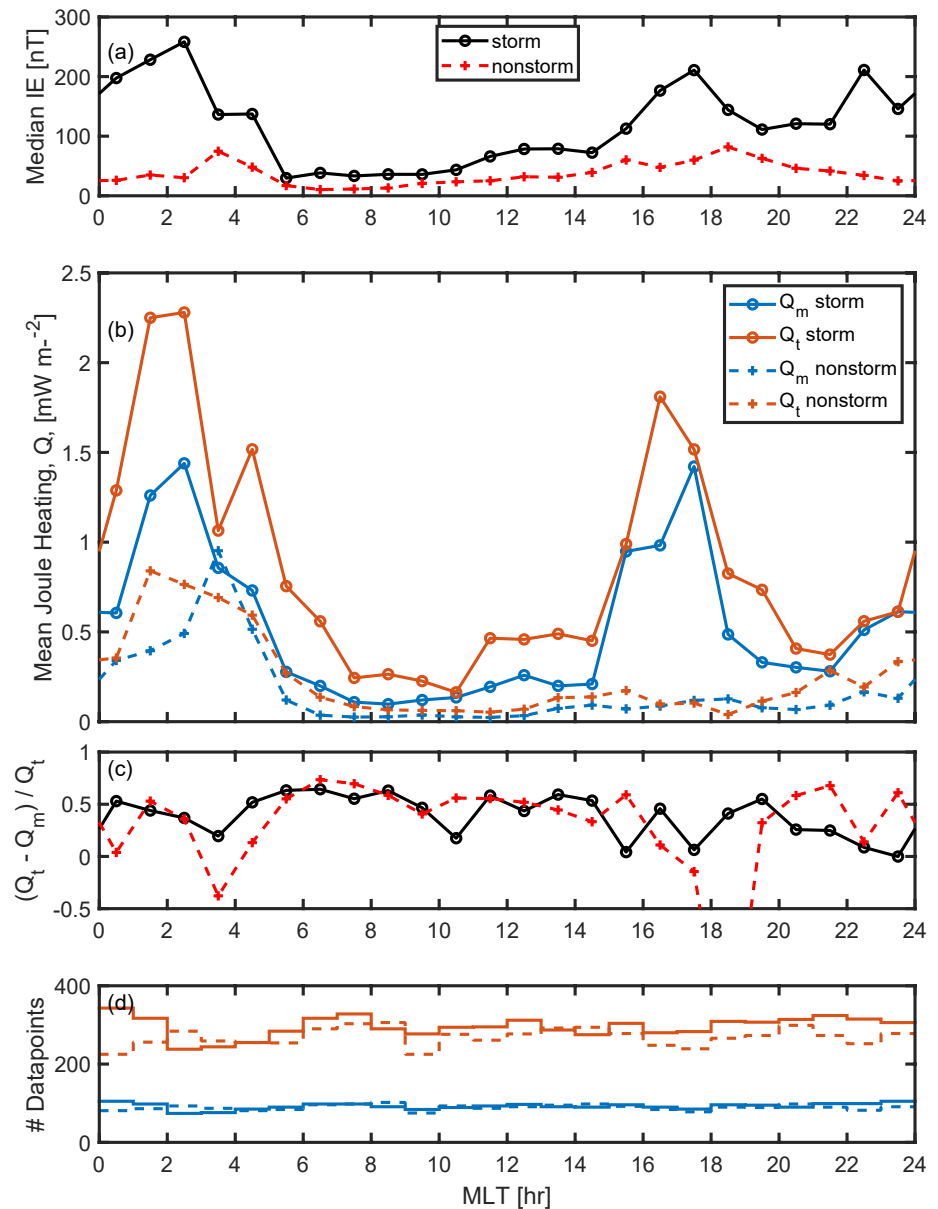
Figure 9. Average of the ionospheric component of Joule heating, Q, as a function of MLT, during the storm and non-storm times of September 2005. Panel (a) gives the median IE index in MLT for the storm (black) and non-storm (periods). Panel (b) shows the monostatic (blue) and tristatic (orange) weighted mean values of Q for storm time (circles) and non-storm time (dashed crosses). Panel (c) is the ratio of the relative difference between Q from the two methods for storm time (black) and non-storm time (red). Panel (d) gives the number of data points that have contributed to the averages for both techniques for storm (solid line) and non-storm times (dashed lines).

relative to the monostatic technique (which was used by Aikio et al. (2012) to determine the neutral winds), the relative difference drops to 46% of Q_t ($Q_m = 0.54\,Q_t$), which is still appreciable.

By integrating Q with respect to time we can determine the difference in total energy between the storm and non-storm periods for both techniques. These numbers are indicative since they ignore the neutral wind, which is important, especially when the geomagnetic activity is low. The inclusion of the neutral wind will modify the overall values of the Joule Heating but will not compensate for the difference. During the storm the estimate from the tristatic method was 5.9 kJ m^{-2} and the monostatic was 4.2 kJ m^{-2}, thus the monostatic technique led to an estimate that was 29% lower than the tristatic across the whole period. For the non-storm period the tristatic gave 2.7 kJ m^{-2} and the monostatic was 1.2 kJ m^{-2}, 56% lower. This indicates that the absolute difference between the

two techniques does not alter much with geomagnetic activity during this period, but the relative difference is higher for less active conditions which is also when the neutral wind effect become even more important (Aikio et al., 2012).

The method of determining the velocity and hence the electric field has an impact on the Joule heating calculation. Where the differences are large, it is the small-scale, rapid tristatic measurement that leads to a higher estimate; in the case that we have looked at this is primarily in the morning sector. This is in line with Rodger et al. (2001), which identified a significant increase in heating when smaller scales were considered. In that study the smaller temporal and spatial scale was comparable with that of the monostatic measurement reported here, such that this work carries the observation to smaller scales and continues to find an overall increase. The measurements presented here are localized but are directly applicable across the auroral zone. The effects of heating spread throughout the atmosphere (e.g., Laskar et al., 2021) and so increase densities and drag across a larger portion of the satellite orbit.

5.4. The Future

The development of EISCAT_3D (McCrea et al., 2015) provides the perfect opportunity to further investigate the effect of scale on the vector measurements of incoherent scatter and how that translates to electrodynamic processes. Since EISCAT_3D will be able to produce multiple, simultaneous, intersecting beams, it will be possible to replicate a monostatic-type measurement at the same cadence as simultaneous tristatic measurements. The large field of view will facilitate multiple tristatic measurements such that a volumetric image of the velocity field will be achieved. This can be directly compared with other parameters (such as the 3-D pattern of electron density and temperature) to establish the impact that different sized structures (such as auroral arcs) have on the local velocity field (and hence the electric field). Careful averaging will allow experiments to be conducted to determine the velocity at various spatial scales (in a similar manner to the tristatic and monostatic comparison) in response to the different structure sizes and establish the impact of both spatial and temporal scales on the magnitudes of the observations.Furthermore, the multi-beam, large volumetric measurements of EISCAT_3D will provide a means of determining the importance of the small-scale differences to the electrodynamics beyond the results shown here. By establishing the spatial distribution of Joule heating and feeding that information into large scale models it will be possible to assess the overall impact and significance.

6. Conclusions

We have used the extensive archive of EISCAT data to compare the ion velocity measurements from the tristatic and monostatic techniques, which derive estimates across different horizontal scales in the F-region. Both represent the large-scale, convection flow with generally good agreement. The biggest differences in local time averages are observed for strongly northward IMF conditions. This is consistent with past observations and could be attributed to stronger solar wind driving (non-northward IMF) reducing the variability.

Even when the large-scale average is close to zero, direct comparison of the velocities shows that there can be significant differences that vary with MLT; up to several 100 ms^{-1} on the night side. The difference between the velocity estimates is correlated with the measure of the variability of the tristatic measurement ($R \sim 0.6$). Differences in the velocity observations are broadly consistent with small scale flow bursts in the ionosphere as reported by previous authors. These may be associated with the flows that accompany enhancements in auroral arcs, explaining the local time variation in the velocity difference distributions. However, this cannot explain all the difference between the techniques and further investigation is required, particularly focused around periods of increased auroral activity.

The different velocity values that are obtained from the monostatic and tristatic measurements can lead to significant differences in the magnitude of the ionospheric component of Joule heating. Using the long CP2 run from EISCAT in September 2005 as a case study we were able to compare the MLT and geomagnetic activity dependence of the Joule heating for a large geomagnetic storm and for a quieter period that followed. Both periods showed the characteristic maximum in the morning sector and in both cases the heating from the tristatic method was greater than that calculated from the monostatic method. Overall, the difference between the two was 45% for storm-time and 48% for the non-storm period, with a greater difference in the morning sector (52%). The neutral

winds would modify this difference depending on MLT and the prevailing geomagnetic conditions. Taking the largest estimate of impact, the morning difference between Q_m and Q_t would be 46% of Q_t.

Thus, the greater temporal variability measured by the tristatic technique at smaller scales ($\sim$10 km compared to $\sim$100 km for the monostatic technique) leads to a moderate increase on the local estimate of Joule heating. This warrants further study to properly establish the cause and to determine whether there is a significant impact on the large-scale energy budget and by extension the impact on thermospheric temperatures and densities during storms.

Data Availability Statement

The analyzed EISCAT data values of velocity, electric field and conductance that were used in this paper are available from the NIPR EISCAT database (http://pc115.seg20.nipr.ac.jp/www/eiscatdata/). Both the tristatic and monostatic velocity data are stored as daily ASCII files. The tristatic data can be accessed at http://pc115. seg20.nipr.ac.jp/www/eiscatdata/vecvel/uhfkst_cp1_cp2_cp3_new/ascii/, and the monostatic data are available at http://pc115.seg20.nipr.ac.jp/www/eiscatdata/vecvel/cp2tro/ant/ascii/. The height integrated conductivity data are also available as ASCII files at http://pc115.seg20.nipr.ac.jp/www/eiscatdata/conductivity/uhf_sigma/2005/. The magnetometer data that underpins the IE index and the index itself are freely available from the IMAGE magnetometer data repository (https://space.fmi.fi/image/) and the data can be accessed via: https://space.fmi. fi/image/www/il_index_panel.php. We thank the institutes who maintain the IMAGE Magnetometer Array: Tromsø Geophysical Observatory of UiT the Arctic University of Norway (Norway), Finnish Meteorological Institute (Finland), Institute of Geophysics Polish Academy of Sciences (Poland), GFZ German Research Centre for Geosciences (Germany), Geological Survey of Sweden (Sweden), Swedish Institute of Space Physics (Sweden), Sodankylä Geophysical Observatory of the University of Oulu (Finland), and Polar Geophysical Institute (Russia). We acknowledge NASA GSFC's Space Physics Data Facility's OMNIWeb service for the use of OMNI data (https://omniweb.gsfc.nasa.gov). The data can be downloaded as yearly ASCII files at: https://spdf. gsfc.nasa.gov/pub/data/omni/high_res_omni/ (Papitashvili & King, 2020). The statistical analysis and plotting in this paper was performed using MATLAB ver. R2020b including the statistics toolboxes, the sanePColor (Manning, 2016) and Wmean (Auton, 2009) functions from file exchange and the Multi Instrument Analysis (MIA) toolbox by Marple and Honary (2004).

References

Abel, G. A., Freeman, M. P., & Chisham, G. (2006). Spatial structure of ionospheric convection velocities in regions of open and closed magnetic field topology. *Geophysical Research Letters*, *33*(24), L24103. https://doi.org/10.1029/2006GL027919

Abel, G. A., Freeman, M. P., & Chisham, G. (2009). IMF clock angle control of multifractality in ionospheric velocity fluctuations. *Geophysical Research Letters*, *36*(19), L19102. https://doi.org/10.1029/2009GL040336

Aikio, A. T., Cai, L., & Nygrén, T. (2012). Statistical distribution of height-integrated energy exchange rates in the ionosphere. *Journal of Geophysical Research*, *117*(A10), A10325. https://doi.org/10.1029/2012JA018078

Aikio, A. T., Vanhamäki, H., Workayehu, A. B., Virtanen, I. I., Kauristie, K., Juusola, L., et al. (2018). Swarm satellite and EISCAT radar observations of a plasma flow channel in the auroral oval near magnetic midnight. *Journal of Geophysical Research: Space Physics*, *123*, 5140–5158. 10.1029/2018JA025409

Aruliah, A. L., Griffin, E. M., Yiu, H.-C. I., McWhirter, I., & Charalambous, A. (2010). Scandi–An all-sky Doppler imager for studies of thermospheric spatial structure. *Annales Geophysicae*, *28*(2), 549–567. https://doi.org/10.5194/angeo-28-549-2010

Auton, A. (2009). *MATLAB Central File Exchange*. Wmean. Retrieved from https://www.mathworks.com/matlabcentral/fileexchange/14416-wmean

Behnke, R. A., & Hagfors, T. (1974). Evidence for the existence of nighttime F-region polarization fields at Arecibo. *Radio Science*, *9*(2), 211–216. https://doi.org/10.1029/RS009i002p00211

Billett, D., Wild, J. A., Grocott, A., Aruliah, A. L., Ronksley, A. M., Walach, M.-T., & Lester, M. (2019). Spatially resolved neutral wind response times during high geomagnetic activity above Svalbard. *Journal of Geophysical Research: Space Physics*, *124*, 6950–6960. 10.1029/2019JA026627

Brekke, A., Nozawa, S., & Sparr, T. (1994). Studies of the E region neutral wind in the quiet auroral ionosphere. *Journal of Geophysical Research*, *99*(A5), 8801–8825. https://doi.org/10.1029/93JA03232

Cai, L., Aikio, A. T., & Nygrén, T. (2014). Solar wind effect on Joule heating in the high-latitude ionosphere. *Journal of Geophysical Research: Space Physics*, *119*(12), 10440–10455. https://doi.org/10.1002/2014JA020269

Chisham, G., Lester, M., Milan, S. E., Freeman, M. P., Bristow, W. A., Grocott, A., et al. (2007). A decade of the super dual auroral radar network (SuperDARN): Scientific achievements, new techniques and future directions. *Surveys in Geophysics*, *28*(1), 33–109. https://doi.org/10.1007/s10712-007-9017-8

Davies, J. A., Lester, M., Milan, S. E., & Yeoman, T. K. (1999). A comparison of velocity measurements from the CUTLASS Finland radar and the EISCAT UHF system. *Annales Geophysicae*, *17*, 892–902. https://doi.org/10.1007/s00585-999-0892-9

Davis, T. N., & Sugiura, M. (1966). Auroral electrojet activity index AE and its universal time variations. *Journal of Geophysical Research*, *71*(3), 785–801. https://doi.org/10.1029/JZ071i003p00785

Deng, Y., Maute, A., Richmond, A. D., & Roble, R. G. (2009). Impact of electric field variability on Joule heating and thermospheric temperature and density. *Geophysical Research Letters*, *36*(8), L08105. https://doi.org/10.1029/2008GL036916

Deng, Y., & Ridley, A. J. (2007). Possible reasons for underestimating Joule heating in global models: E field variability, spatial resolution, and vertical velocity. *Journal of Geophysical Research*, *112*(A9), A09308. https://doi.org/10.1029/2006JA012006

Dungey, J. W. (1961). Interplanetary magnetic field and the auroral zones. *Physical Review Letters*, *6*(2), 47–48. https://doi.org/10.1103/physrevlett.6.47

Foster, J. C. (1983). An empirical electric field model derived from Chatanika radar data. *Journal of Geophysical Research*, *88*(A2), 981–987. https://doi.org/10.1029/JA088iA02p00981

Freeman, M. P., Farrugia, C. J., Burlaga, L. F., Hairston, M. R., Greenspan, M. E., Ruohoniemi, J. M., & Lepping, R. P. (1993). The interaction of a magnetic cloud with the Earth: Ionospheric convection in the northern and southern hemispheres for a wide range of quasi-steady interplanetary magnetic field conditions. *Journal of Geophysical Research*, *98*(A5), 7633–7655. https://doi.org/10.1029/92JA02350

Fujii, R., Nozawa, S., Buchert, S. C., & Brekke, A. (1999). Statistical characteristics of electromagnetic energy transfer between the magnetosphere, the ionosphere, and the thermosphere. *Journal of Geophysical Research*, *104*(A2), 2357–2365. https://doi.org/10.1029/98JA02750

Gillies, R. G., Hussey, G. C., Sofko, G. J., Wright, D. M., & Davies, J. A. (2010). A comparison of EISCAT and SuperDARN *F*-region measurements with consideration of the refractive index in the scattering volume. *Journal of Geophysical Research*, *115*, A06319. https://doi.org/10.1029/2009JA014694

Grocott, A., Yeoman, T. K., Nakamura, R., Cowley, S. W. H., Frey, H. U., Rème, H., & Klecker, B. (2004). Multi-instrument observations of the ionospheric counterpart of a bursty bulk flow in the near-Earth plasma sheet. *Annales Geophysicae*, *22*(4), 1061–1075. https://doi.org/10.5194/angeo-22-1061-2004

Gustafsson, G., Boström, R., Holback, B., Holmgren, G., Lundgren, A., Stasiewicz, K., et al. (1997). The electric field and wave experiment for the cluster mission. *Space Science Reviews*, *79*, 137–156. 10.1023/A:1004975108657

Hagfors, T., & Behnke, R. A. (1974). Measurements of three-dimensional plasma velocities at Arecibo. *Radio Science*, *92*(A4), 3345–3355.

Hanuise, C., Senior, C., Cerisier, J.-C., Villain, J.-P., Greenwald, R. A., Ruohoniemi, J. M., & Baker, K. B. (1993). Instantaneous mapping of high-latitude convection with coherent HF radars. *Journal of Geophysical Research*, *98*(A10), 17387–17400. https://doi.org/10.1029/93JA00813

Heinselman, C. J., & Nicolls, M. J. (2008). A Bayesian approach to electric field and E-region neutral wind estimation with the Poker Flat Advanced Modular incoherent scatter radar. *Radio Science*, *43*(5), RS5013. https://doi.org/10.1029/2007RS003805

Hosokawa, K., & Ogawa, Y. (2010). Pedersen current carried by electrons in auroral D-region. *Geophysical Research Letters*, *37*(18), L18103. https://doi.org/10.1029/2010GL044746

Khan, H., & Cowley, S. W. H. (1999). Observations of the response time of high-latitude ionospheric convection to variations in the interplanetary magnetic field using EISCAT and IMP-8 data. *Annales Geophysicae*, *17*, 1306–1335. https://doi.org/10.1007/s00585-999-1306-8

King, J. H., & Papitashvili, N. E. (2005). Solar wind spatial scales in and comparisons of hourly Wind and ACE plasma and magnetic field data. *Journal of Geophysical Research*, *110*(A2), A02104. https://doi.org/10.1029/2004JA010649

Laskar, F. I., Eastes, R. W., Codrescu, M. V., Evans, J. S., Burns, A. G., Wang, W., et al. (2021). Response of GOLD retrieved thermospheric temperatures to geomagnetic activities of varying magnitudes. *Geophysical Research Letters*, *48*(15), e2021GL093905. https://doi.org/10.1029/2021GL093905

Lehtinen, M. S., & Huuskonen, A. (1996). General incoherent scatter analysis and GUISDAP. *Journal of Atmospheric and Terrestrial Physics*, *58*(1–4), 435–452. https://doi.org/10.1016/0021-9169(95)00047-X

Lühr, H., Aylward, A., Bucher, S. C., Pajunpää, A., Pajunpää, K., Holmboe, T., & Zalewski, S. M. (1998). Westward moving dynamic substorm features observed with the IMAGE magnetometer network and other ground based instruments. *Annales Geophysicae*, *16*(4), 425–440. https://doi.org/10.1007/s00585-998-0425-y

Manning, J. (2016). sanePColor(varargin), MATLAB central file exchange. Retrieved from https://uk.mathworks.com/matlabcentral/fileexchange/35601-sanepcolor-varargin?s_tid=srchtitle

Marple, S., & Honary, F. (2004). A multi-instrument data analysis toolbox. *Advances in Polar Upper Atmosphere Research*, *18*, 120–130.

McCrea, I., Aikio, A., Alfonsi, L., Belova, E., Buchert, S., Clilverd, M., et al. (2015). The science case for the EISCAT_3D radar. *Progress in Earth and Planetary Science*, *2*, 21. 10.1186/s40645-015-0051-8

Nozawa, S., & Brekke, A. (2000). A case study of the auroral E region neutral wind on a quiet summer day: Comparison of the European Incoherent Scatter UHF radar for deriving the E region wind. *Radio Science*, *35*(3), 845–863. https://doi.org/10.1029/1999RS002166

Nygrén, T., Aikio, A. T., Kuula, R., & Voiculescu, M. (2011). Electric fields and neutral winds from monostatic incoherent scatter measurements by means of stochastic inversion. *Journal of Geophysical Research*, *116*(A5), A05305. https://doi.org/10.1029/2010JA016347

Papitashvili, N. E., & King, J. H. (2020). OMNI 1-min data. [Dataset]. NASA Space Physics Data Facility. 10.48322/45bb-8792

Rich, F. J., & Hairston, M. (1994). Large-scale convection patterns observed by DMSP. *Journal of Geophysical Research*, *99*(A3), 3827–3844. https://doi.org/10.1029/93JA03296

Rishbeth, H., & van Eyken, A. P. (1993). Eiscat: Early history and the first ten years of operation. *Journal of Atmospheric and Terrestrial Physics*, *55*(4–5), 525–542. https://doi.org/10.1016/0021-9169(93)90002-G

Rishbeth, H., & Williams, P. J. S. (1985). The EISCAT ionospheric radar: The system and its early results. *Quarterly Journa of the Royal Astronomical Society*, *26*, 478–512.

Rodger, A. S., Wells, G. D., Moffett, R. J., & Bailey, G. J. (2001). The variability of Joule heating, and its effects on the ionosphere and thermosphere. *Annales Geophysicae*, *19*(7), 773–781. https://doi.org/10.5194/angeo-19-773-2001

Ruohoniemi, J. M., & Baker, K. B. (1998). Large-scale imaging of high-latitude convection with Super Dual Auroral Radar Network HF radar observations. *Journal of Geophysical Research*, *103*(A9), 20797–20811. https://doi.org/10.1029/98JA01288

Ruohoniemi, J. M., & Greenwald, R. A. (2005). Dependencies of high-latitude plasma convection: Consideration of interplanetary magnetic field, seasonal, and universal time factors in statistical patterns. *Journal of Geophysical Research*, *110*(A9), A09204. https://doi.org/10.1029/2004JA010815

Senior, A., Kavanagh, A. J., Kosch, M. J., & Honary, F. (2007). Statistical relationships between cosmic radio noise absorption and ionospheric electrical conductances in the auroral zone. *Journal of Geophysical Research*, *112*(A11), A11301. https://doi.org/10.1029/2007JA012519

Strangeway, R. J. (2012). The equivalence of Joule dissipation and frictional heating in the collisional ionosphere. *Journal of Geophysical Research*, *117*(A2), A02310. https://doi.org/10.1029/2011JA017302

Thayer, J. P. (1998). Height-resolved Joule heating rates in the high-latitude E region and the influence of neutral winds. *Journal of Geophysical Research*, *103*(A1), 471–487. https://doi.org/10.1029/97JA02536

Thébault, E., Finlay, C. C., Beggan, C. D., Alken, P., Aubert, J., Barrois, O., et al. (2015). International geomagnetic reference field: The 12th generation. *Earth Planets and Space*, *67*(1), 79. https://doi.org/10.1186/s40623-015-0228-9

Trattner, K. J., Fuselier, S. A., Petrinec, S. M., Yeoman, T. K., Mouikis, C., Kucharek, H., & Reme, H. (2005). Reconnection sites of spatial cusp structures. *Journal of Geophysical Research*, *110*(A4), A04207. https://doi.org/10.1029/2004JA010722

Tsunoda, R. T. (1988). High-latitude F region irregularities: A review and synthesis. *Reviews of Geophysics*, *26*(4), 719–760. https://doi.org/10.1029/RG026i004p00719

Tsurutani, B. T., Gonzalez, W. D., Gonzalez, A. L. C., Guarnieri, F. L., Gopalswamy, N., Grande, M., et al. (2006). Corotating solar wind streams and recurrent geomagnetic activity: A review. *Journal of Geophysical Research*, *111*(A7), A07S01. https://doi.org/10.1029/2005JA011273

Vasyliunas, V. M., & Song, P. (2005). Meaning of ionospheric Joule heating. *Journal of Geophysical Research*, *110*(A2), A02301. https://doi.org/10.1029/2004JA010615

Williams, P. J. S., Etemadi, A., McCrea, I. W., & Todd, H. (1996). Errors due to random noise in velocity measurement using incoherent-scatter radar. *Annales Geophysicae*, *14*(12), 1480–1486. https://doi.org/10.1007/s00585-996-1480-x

Williams, P. J. S., Jones, G. O. L., & Jain, A. R. (1984). Methods of measuring plasma velocity with EISCAT. *Journal of Atmospheric and Terrestrial Physics*, *46*(6–7), 521–530. https://doi.org/10.1016/0021-9169(84)90071-0

Williams, P. J. S., Virdi, T. S., & Cowley, S. W. H. (1989). Substorm processes in the geomagnetic tail and their effect in the nightside auroral zone ionosphere as observed by EISCAT. *Philosophical Transactions of the Royal Society of London A*, *328*, 173–193. https://doi.org/10.1098/rsta.1989.0030

Williams, P. J. S., Virdi, T. S., Cowley, S. W. H., & Lester, M. (1990). Short-lived bursts of plasma velocity in the auroral zone. I. Observational evidence from radar measurements. *Journal of Atmospheric and Terrestrial Physics*, *52*(6–8), 421–430. https://doi.org/10.1016/0021-9169(90)90041-K

Wright, J. W., & Pitteway, M. L. V. (1979a). Real-time data acquisition and interpretation capabilities of the Dynasonde: 1. Data acquisition and real-time display. *Radio Science*, *14*(5), 815–825. https://doi.org/10.1029/RS014i005p00815

Wright, J. W., & Pitteway, M. L. V. (1979b). Real-time data acquisition and interpretation capabilities of the Dynasonde: 2. Determination of magnetoionic mode and echolocation using a small spaced receiving array. *Radio Science*, *14*(5), 827–835. https://doi.org/10.1029/RS014i005p00827

Zhang, S.-R., Holt, J. M., & McCready, M. (2007). High latitude convection based on long-term incoherent scatter radar observations in North America. *Journal of Atmospheric and Solar-Terrestrial Physics*, *69*(10–11), 1273–1291. https://doi.org/10.1016/j.jastp.2006.08.017

Zou, S., Lyons, L. R., Nicolls, M. J., & Heinselman, C. J. (2009). PFISR observations of strong azimuthal flow bursts in the ionosphere and their relation to nightside aurora. *Journal of Atmospheric and Solar-Terrestrial Physics*, *71*(6–7), 729–737. https://doi.org/10.1016/j.jastp.2008.06.015